



HAL
open science

Detection and modelling of CH₃NC in TMC-1

Jessica Tennis, Ci Xue, Dahbia Talbi, P Bryan Changala, Madelyn Sita, Brett McGuire, Eric Herbst

► **To cite this version:**

Jessica Tennis, Ci Xue, Dahbia Talbi, P Bryan Changala, Madelyn Sita, et al.. Detection and modelling of CH₃NC in TMC-1. *Monthly Notices of the Royal Astronomical Society*, 2023, 525 (2), pp.2154-2171. 10.1093/mnras/stad2398 . hal-04190563

HAL Id: hal-04190563

<https://hal.science/hal-04190563>

Submitted on 25 Jan 2024

HAL is a multi-disciplinary open access archive for the deposit and dissemination of scientific research documents, whether they are published or not. The documents may come from teaching and research institutions in France or abroad, or from public or private research centers.

L'archive ouverte pluridisciplinaire **HAL**, est destinée au dépôt et à la diffusion de documents scientifiques de niveau recherche, publiés ou non, émanant des établissements d'enseignement et de recherche français ou étrangers, des laboratoires publics ou privés.

Detection and Modelling of CH₃NC in TMC-1

Jessica D. Tennis,^{1*} Ci Xue,² Dahbia Talbi,³ P. Bryan Changala,⁴ Madelyn L. Sita,¹
Brett McGuire,^{2,5} Eric Herbst,^{1,6}

¹*Department of Chemistry, University of Virginia, Charlottesville, VA 22904, USA*

²*Department of Chemistry, Massachusetts Institute of Technology, Cambridge, MA 02139, USA*

³*Université de Montpellier UMR5299-CNRS-Université de Montpellier, France*

⁴*Center for Astrophysics | Harvard & Smithsonian, Cambridge, MA 02138, USA*

⁵*National Radio Astronomy Observatory, Charlottesville, VA 22903, USA*

⁶*Department of Astronomy, University of Virginia, Charlottesville, VA 22904, USA*

Accepted XXX. Received YYY; in original form ZZZ

ABSTRACT

Two closely related isomeric pairs of cyanides, CH₃[CN/NC] and H₂C[CN/NC], are studied in cold, dark interstellar cloud conditions. In contrast to the diverse detections of methyl cyanide (CH₃CN) in space, methyl isocyanide (CH₃NC) has previously only been observed in warm and hot star-forming regions. We report the detection of CH₃NC in the cold prestellar core TMC-1 using the Green Bank Telescope with a detection significance of 13.4 σ . Hyperfine transitions in H₂CCN and quadrupole interactions in CH₃CN and CH₃NC were matched to a spectral line survey from the GOTHAM large project on the Green Bank Telescope, resulting in abundances with respect to hydrogen of $1.92_{-0.07}^{+0.13} \times 10^{-9}$ for the cyanomethyl radical (H₂CCN), $5.02_{-2.06}^{+3.08} \times 10^{-10}$ for CH₃CN, and $2.97_{-1.37}^{+2.10} \times 10^{-11}$ for CH₃NC. Efforts to model these molecules with the three-phase gas-grain code *Nautilus* in TMC-1 conditions overproduce both CH₃CN and CH₃NC, though the ratio of $\sim 5.9\%$ is consistent across observations and models of these species. This may point to missing destruction routes in the model. The models capture the larger abundance of H₂CCN well. Dissociative recombination is found to be the primary production route for these molecules, and reactions with abundant ions are found to be the primary destruction routes. H + CH₃NC is investigated with transition state theory as a potential destruction route, but found to be too slow in cold cloud conditions to account for the discrepancy in modelled and observed abundances of CH₃NC.

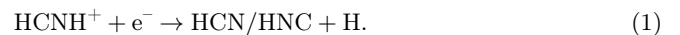
Key words: ISM:molecules – ISM:abundances – molecular processes

1 INTRODUCTION

One of the very first molecules to be detected in interstellar space was hydrogen cyanide (HCN), followed the next year by hydrogen isocyanide (HNC) (Snyder & Buhl 1971, 1972). Since then, cyanides and isocyanides have been detected in diverse interstellar environments (McGuire 2022, and references therein), and the ratio of isocyanides to their cyanide isomers has been the topic of much investigation (e.g. Irvine & Schloerb 1984; Graninger et al. 2015; Willis et al. 2020; Xue et al. 2020). A cyanide is any molecule with a terminal -CN group, and an isocyanide is any molecule with a terminal -NC group. As Remijan et al. (2005) points out, however, the interstellar medium is too cold for unimolecular interconversion between cyanides and isocyanides, so the ratio reflects differences in the formation and destruction processes for each rather than the ratio of thermodynamic stabilities.

For the HCN/HNC case, for example, Graninger et al. (2014) find that reaction kinetics explain the observed ratio

in the giant molecular cloud Orion Molecular Cloud-1 (OMC-1). The HNC:HCN ratio is 1:80 at the core of OMC-1 and grows to unity at the coldest, outermost edges (Schilke et al. 1992) because in this latter temperature regime dissociative recombination, the gas-phase reaction between a positive ion and an electron to form two or more neutral fragments, produces nearly equal amounts of the two isomers, as:



The ratio is lower at the core of OMC-1 than at its edge due to the reaction



which destroys HNC in favor of HCN. Reaction 2 has an energy barrier which makes this reaction more efficient at higher temperatures, and therefore allows the abundance of the product HCN to be higher at higher temperatures as compared to the reactant HNC (Graninger et al. 2014).

CH₃CN has been seen in almost every type of interstellar environment (Cernicharo et al. 1988; Purcell et al. 2006; Girard et al. 2012; Gratier et al. 2013), but its isomer CH₃NC,

* E-mail: jdt6mp@virginia.edu (JDT)

9486 cm⁻¹ higher in energy (Remijan et al. 2005), has only been detected in molecular hot cores and photodissociation regions (Willis et al. 2020; Gratier et al. 2013). CH₃NC is difficult to detect because it is less abundant, as we show. CH₃CN and CH₃NC are also mainly produced by the dissociative recombination mechanism. We investigate the barrier height of the analogous



reaction to assess the viability of these isomers as a tracer of kinetic gas temperatures, and test the effects of this reaction on their abundances in kinetic models.

Here, in Section 2 we report the detection of CH₃NC, CH₃CN and H₂CCN toward the Taurus Molecular Cloud (hereafter referred to as TMC-1) - a dark, cold molecular cloud at a distance of 150 pc. We then calculate the potential energy surface for the reaction between CH₃NC and the H atom in Section 3 and detail efforts to model the abundance of CH₃NC, CH₃CN, H₂CCN, and H₂CNC in cold, dark cloud conditions in Section 4. We discuss those results in Section 5 before reaching our conclusions in Section 6.

2 OBSERVATIONS

The observations were performed with the Robert C. Byrd 100-m Green Bank Telescope of the large observational program GOTHAM (Green Bank Telescope Observations of TMC-1: Hunting for Aromatic Molecules), directed toward the TMC-1 cyanopolyne peak (CP) centered at $\alpha_{\text{J2000}} = 04^{\text{h}}41^{\text{m}}42^{\text{s}}.5$, $\delta_{\text{J2000}} = 25^{\circ}41'26''.8$. The first three data reductions of the GOTHAM program (hereafter referred as DR1, DR2, and DR3) comprise observations obtained between February 2018 - May 2019 (DR1), - June 2020 (DR2), and - April 2021 (DR3). Detailed information concerning the GOTHAM observations and the data calibration can be found in McGuire et al. (2020, 2021). The GOTHAM observations used here are the fourth data reduction with completed observations through May 2022 (hereafter referred as DR4), which extended the frequency coverage to 7.906 - 36.411 GHz with a few gaps and improved the sensitivity in some frequency coverage already covered by previous data release Sita et al. (2022). The beam size varies between $\sim 90''$ at 8 GHz and $\sim 20''$ at 36 GHz. At a uniform 0.05 km s⁻¹ velocity resolution, the RMS noise ranges from $\sim 2 - 20$ mK across the dataset.

As shown in the left panel of Figure 1, we identified three hyperfine components of the CH₃NC 1₀ - 0₀ transition. The strongest line has a peak intensity of 14.6 mK, corresponding to 5.8 σ . To assess the statistical significance of the detection, we construct a composite line profile with the best-fit parameters and use it as a matched filter to perform the cross-correlation. The result is shown in the right panel of Figure 1, and indicates a significance to the detection of CH₃NC of 13.4 σ . The ¹⁴N nuclear electric quadrupole splittings are the only hyperfine structure resolvable for the closed-shell species, CH₃CN and CH₃NC. Figure 2 shows the individual line detections of CH₃CN in the GOTHAM DR 4 data. The open-shell H₂CCN radical has more extensive hyperfine structure owing to magnetic interactions of the electronic and nuclear spins. We detect 25 resolved hyperfine components of its 1_{0,1} - 0_{0,0} transition with GOTHAM. The spectroscopic

details of the observed hyperfine transitions are listed in Appendix A.

Because the hyperfine states differ in energy by only a few mK, the detected lines cannot constrain T_{ex} . In contrast, the carbon-chain molecule HC₉N has bright lines in the observed spectra, and the transitions of HC₉N with a wide range of energy levels are covered by the GOTHAM data. As such, the source properties of HC₉N provide prior information about that of other highly polar, prolate molecular species in TMC-1 (Loomis et al. 2021). In this study, we assume the T_{ex} of the three species to be 6.7 K, considering that the posterior of T_{ex} for HC₉N is 6.7 \pm 0.1 K (Loomis et al. 2021) and that of HC₄NC, another isocyanide molecule detected in this region, is 6.7 \pm 0.3 K (Xue et al. 2020).

In order to constrain molecular excitation conditions and explore the parameter space, we used the same Markov-Chain Monte Carlo (MCMC) model employed in other GOTHAM analyses (e.g. McGuire et al. 2020; Xue et al. 2020; Lee et al. 2021; Sita et al. 2022). The technique is described in detail in Loomis et al. (2021), and a rigorous analysis of potential sources of errors, uncertainties, and spurious signals is described in the Supplementary Information for McGuire et al. (2021). Previous observations both from GOTHAM (Loomis et al. 2021) and others (Dobashi et al. 2018) have found that most emission seen at centimeter wavelengths toward TMC-1 can be separated into contributions from four distinct velocity components within the larger structure, at approximately 5.6, 5.8, 5.9, and 6.0 km s⁻¹. In this study, a uniform T_{ex} and line width (ΔV) for each velocity component are assumed, while source velocity (V_{lsr}), source size ($''$), and column density (N_T) are variable among different velocity components. Therefore, there are a total of 13 free parameters used to describe the molecular emission features observed in the observation data and adjusted in the MCMC analysis. A forward model with 13 free parameters is used to generate iteratively model spectra which are compared with the observations. Posterior probability distributions for each parameter and their co-variances are generated with 100 walkers and 10⁵ draws, populating the corner plots in Appendix B. The resulting best-fitting parameters of each velocity component are summarized in Table 1 for CH₃NC, Table 2 for CH₃CN, and Table B1 for H₂CCN. We adopt the 50th percentile value of the posterior probability distributions as the representative value of each parameter for the molecule, and use the 16th and 84th percentile values for the uncertainties. For probabilities that show a Gaussian distribution, these correspond to the 1 σ uncertainty level. Many of our resulting probability distributions are indeed either Gaussian or nearly Gaussian, and thus these values are usually quite representative of the 1 σ uncertainties.

A total column density N_T of 2.97 $^{+2.10}_{-1.37} \times 10^{11}$ cm⁻² is determined for CH₃NC, which corresponds to an abundance with respect to hydrogen of $\sim 3 \times 10^{-11}$, and 5.02 $^{+3.08}_{-2.06} \times 10^{12}$ cm⁻² for CH₃CN, which corresponds to an abundance with respect to hydrogen of $\sim 5 \times 10^{-10}$. Thus, the resultant [CH₃NC]:[CH₃CN] column density ratio is 5.9 $^{+11.2}_{-3.9}$ %. A total N_T of 1.92 $^{+0.13}_{-0.07} \times 10^{13}$ cm⁻² is determined for H₂CCN, which corresponds to an abundance with respect to hydrogen of $\sim 2 \times 10^{-9}$. Similar to H₂CCN, both ¹H and ¹⁴N hyperfine splitting of H₂CNC are resolvable with GOTHAM observations. We generated its hyperfine catalog by refitting the experimental line frequencies reported in Hirao et al.

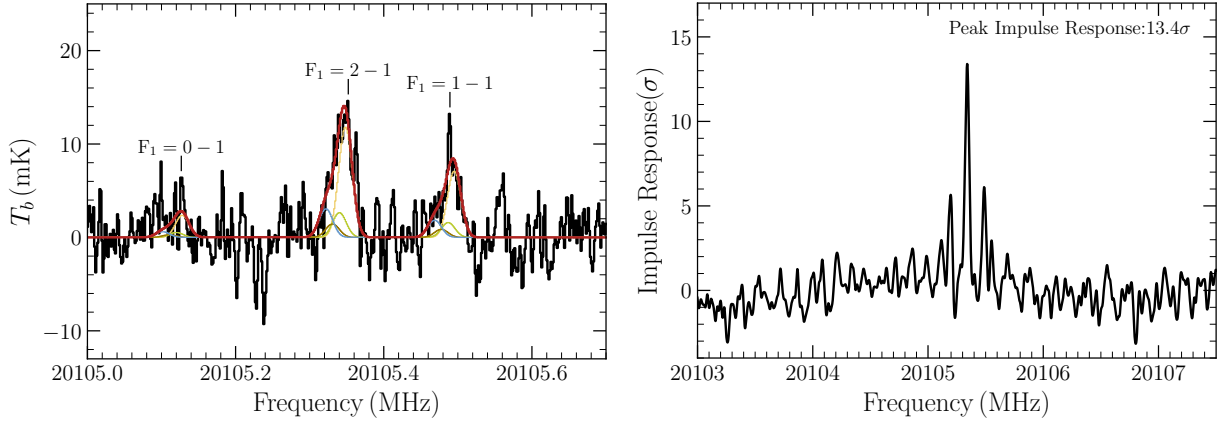


Figure 1. Left: individual line detections of CH_3NC $1_0 - 0_0$ transitions in the GOTHAM DR 4 data. The observed spectra are displayed in black while the best-fitting model to the data, including all velocity components, is overlaid in red. Simulated spectra of the individual velocity components are shown in: yellow (5.65 km s^{-1}), lime (5.77 km s^{-1}), brown (5.91 km s^{-1}), and blue (6.05 km s^{-1}). See Table 1. Right: impulse response function of the observed spectrum using the simulated line profile as a matched filter. The peak of the impulse response function provides a detection significance of 13.4σ . Additionally, the pronounced secondary peaks correspond to the correlations between mismatched simulated and observed spectral components, for example when the simulated $F_1 = 1 - 1$ component overlaps with the observed $F_1 = 2 - 1$ component.

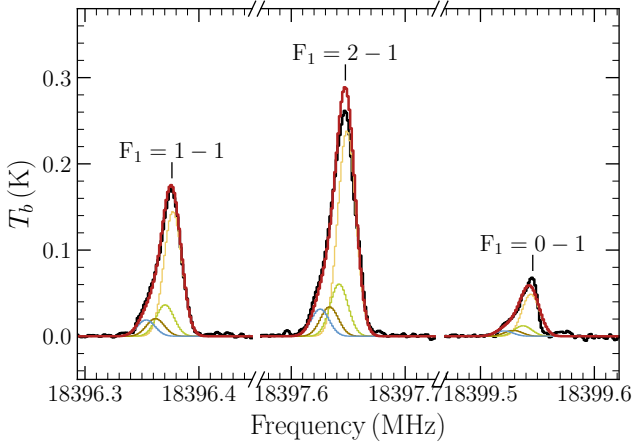


Figure 2. Individual line detections of CH_3CN $1_0 - 0_0$ transitions in the GOTHAM DR 4 data. The observed spectra are displayed in black while the best-fitting model to the data, including all velocity components, is overlaid in red. Simulated spectra of the individual velocity components are shown in: yellow (5.66 km s^{-1}), lime (5.77 km s^{-1}), brown (5.91 km s^{-1}), and blue (6.05 km s^{-1}). See Table 2.

(2007). Its $1_{0,1} - 0_{0,0}$ transitions at 22.2 GHz are covered with GOTHAM’s frequency range. Unfortunately, no lines of H_2CNC were detected above a 3σ detection limit even with match filtering. We used the rms noise level from the 22.2-GHz passband to set an upper limit on the column density N_T of $3.61 \times 10^{11} \text{ cm}^{-2}$ for H_2CNC , which corresponds to an abundance with respect to hydrogen of $\sim 4 \times 10^{-11}$ and a 3σ upper limit of $< 2\%$ is found for the $[\text{H}_2\text{CNC}]:[\text{H}_2\text{CCN}]$ ratio.

3 CALCULATIONS

Understanding the abundance of CH_3NC in TMC-1 requires understanding how it reacts with other species in the cloud, including highly abundant H. The lowest energy path for the reaction between CH_3NC and the H atom was investigated using Density Functional Theory (DFT) and Gaussian 16 (Frisch et al. 2016). The M062X hybrid functional (Zhao & Truhlar 2008) was combined with a correlation-consistent polarized valence quadruple-zeta basis set and augmented by diffuse functions: aug-cc-pVQZ (Gonzalez & Schlegel 1989, 1990), was used. The M062X functional was chosen for its better ability to describe noncovalent bonds (Peverati & Truhlar 2014) and therefore transition states or loose complexes. Structures at minima and maxima (transition states) on the reaction path were located by optimization using analytical gradients. The character of each structure was confirmed by a vibrational analysis carried out at the same theoretical level making use of analytical second-derivative methods. The assignment of the saddle points was confirmed using intrinsic reaction coordinate calculations. For accurate energies, the stationary points (minima and transition states) were recalculated with the explicitly correlated (F12) version of the unrestricted coupled-cluster method with singles, doubles, and perturbative triples, i.e. UCCSD(T)-F12 (Knizia et al. 2009) as implemented in the MOLPRO computer code (Werner et al. 2012; Werner et al. 2020). The correlation-consistent polarized valence quadruple-zeta basis set with F12 optimized, cc-pVQZ-F12 (Peterson et al. 2008), was used for these single-point calculations. All UCCSD(T)-F12/cc-pVQZ-F12//M062X/aug-cc-pVQZ energies were corrected for unscaled zero-point energies calculated at the M062X/aug-cc-pVQZ level. The lowest energy profile obtained can be viewed in Figure 3.

Table 1. CH₃NC best-fit parameters from the MCMC analysis

Component	v_{lsr} (km s ⁻¹)	Size ($''$)	N_T (10 ¹¹ cm ⁻²)	T_{ex} (K)	ΔV (km s ⁻¹)
C1	$5.653^{+0.026}_{-0.036}$	205^{+135}_{-130}	$1.85^{+0.51}_{-0.54}$		
C2	$5.774^{+0.012}_{-0.012}$	189^{+146}_{-138}	$0.42^{+0.80}_{-0.34}$	[6.7]	$0.322^{+0.039}_{-0.037}$
C3	$5.913^{+0.026}_{-0.027}$	185^{+150}_{-140}	$0.23^{+0.48}_{-0.17}$		
C4	$6.045^{+0.012}_{-0.012}$	198^{+141}_{-137}	$0.48^{+0.32}_{-0.32}$		
N_T (Total)		$2.97^{+2.10}_{-1.37} \times 10^{11}$ cm ⁻²			

Notes. The quoted uncertainties represent the 16th and 84th percentile (1σ for a Gaussian distribution) uncertainties. Uncertainties of the total column density were derived by adding the uncertainties of the individual components in quadrature.

Table 2. CH₃CN best-fitting parameters from the MCMC analysis

Component	v_{lsr} (km s ⁻¹)	Size ($''$)	N_T (10 ¹² cm ⁻²)	T_{ex} (K)	ΔV (km s ⁻¹)
C1	$5.662^{+0.023}_{-0.030}$	209^{+133}_{-131}	$3.30^{+0.94}_{-0.89}$		
C2	$5.774^{+0.012}_{-0.011}$	192^{+145}_{-138}	$0.83^{+1.13}_{-0.62}$	[6.7]	$0.299^{+0.047}_{-0.046}$
C3	$5.911^{+0.026}_{-0.026}$	188^{+146}_{-140}	$0.46^{+0.59}_{-0.30}$		
C4	$6.045^{+0.012}_{-0.012}$	190^{+145}_{-139}	$0.43^{+0.42}_{-0.25}$		
N_T (Total)		$5.02^{+3.08}_{-2.06} \times 10^{12}$ cm ⁻²			

Notes. Similar to Table 1.

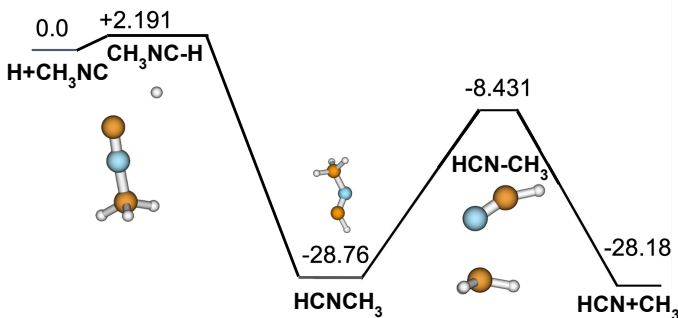


Figure 3. The potential energy surface for the reaction between the H atom and CH₃NC. Relative energies are in kcal/mol. See text for calculation details.

4 ASTROCHEMICAL MODEL

In this work, we use *Nautilus* (version 1.1) (Rauud et al. 2016) to model the abundances of chemical species in the cold, dark cloud conditions appropriate to TMC-1, including a visual extinction A_v of 10, a temperature of 10 K, and a cosmic-ray ionisation rate ζ of 1.3×10^{-17} (see, for example, Wakelam & Herbst (2008)); following Hincelin et al. (2011)

and Loomis et al. (2021) the age of TMC-1 is taken to be $\sim 5 \times 10^5$ years.

Nautilus is a three-phase rate equation model, our version of which includes the rates of 7981 gas-phase reactions and 8034 grain reactions involving 549 gas-phase and 1017 grain-surface and bulk species to compute abundances of species over time, beginning with atoms for all elements except hydrogen, which is dominated by H₂. We added two new species, CH₃NC and CH₂CHNC, as well as the precursor radicals and cations that lead to their formation.

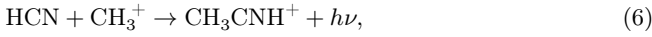
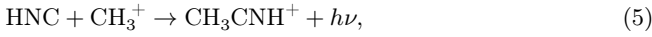
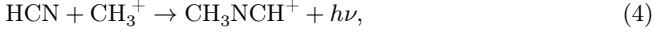
A list of the reactions added is available in Appendix C. This table includes the H+CH₃NC reaction considered in Section 3, the other gas-phase reactions relevant to CH₃NC, H₂CCN, H₂CNC, and the surface neutral-neutral reactions of these species. The standard adsorption, desorption, and mixing of molecules exchanging between the topmost surface layers of ice and the bulk layers below are also included in the reaction network, though the table does not note these. Also omitted from the table are the grain-surface photodestruction reactions. These reactions represent our effort to include CH₃NC in *Nautilus* accurately, with precursor radicals and other potential products from these radicals such as C₂H₃[CN/NC] and C₂H₅[CN/NC], as shown in Table C1. The dominant production and destruction reactions for CH₃CN, CH₃NC, H₂CCN, and H₂CNC are gas-phase in our models.

The resulting CH₃NC abundance with respect to hydrogen under TMC-1 conditions at $\sim 5 \times 10^5$ years is 2.48×10^{-10} ,

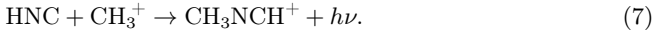
which is about 5% of the CH_3CN abundance, 5.05×10^{-9} . The resulting H_2CCN abundance is 4.92×10^{-9} , and the resulting H_2CNC abundance is 3.64×10^{-9} .

4.1 Radiative Association

Because CH_3CNH^+ and CH_3NCH^+ precede the main production mechanism for the species of interest, it is helpful to consider their production. These ions come from the four related gas-phase radiative association reactions of HCN or HNC with CH_3^+ :



and



The abundance of reactant HCN in TMC-1 in our model is 5.0×10^{-8} with respect to hydrogen at $\sim 5 \times 10^5$ years, in agreement with the observations of [Irvine & Schloerb \(1984\)](#), who find an abundance of 5.0×10^{-8} to 5.0×10^{-9} . The abundance of reactant HNC in our models is 4.8×10^{-8} with respect to hydrogen at the same time, in line with the near-unity HNC:HCN ratio ([Irvine & Schloerb 1984](#); [Loison et al. 2014](#)). The abundance of CH_3^+ in our model is 1.5×10^{-11} . This set of reactions was studied by [Defrees et al. \(1985\)](#), who found that its two products, CH_3CNH^+ and CH_3NCH^+ , are formed in a ratio of 85:15 due to unimolecular isomerization. Later, [Anicich et al. \(1995\)](#) examined the experimental literature on these reactions and determined a total radiative association rate coefficient of $2 \times 10^{-10} \text{ cm}^3 \text{ s}^{-1}$ for Reactions 4 and 6.

Although the rate coefficients of $1.7 \times 10^{-10} (T/300\text{K})^{-3}$ for Reactions 4 and 5, and $3.0 \times 10^{-11} (T/300\text{K})^{-3}$ for Reactions 6 and 7 from [Anicich et al. \(1995\)](#) and [Defrees et al. \(1985\)](#) is used throughout this work, we tested the effects of lowering the rate coefficients, as shown in Figures 4 and 5. At $\sim 5 \times 10^5$ years ([Hincelin et al. 2011](#); [Loomis et al. 2021](#)), Figure 4 shows that the observed abundances of CH_3CN and CH_3NC match the modelled abundance when the rate coefficients for this set of reactions (Reactions 4 - 7) in TMC-1 conditions are between one and two orders of magnitude lower than previously modelled. Figure 5, similarly, shows that the modelled abundance of H_2CCN more closely matches the observed abundance of H_2CCN when the rate coefficients for this set of reactions is between one and two orders of magnitude lower than previously modelled. Further, detailed study of Reactions 4 - 7 is necessary to further constrain the true rate coefficients. All models of various precursor production efficiencies indicate the same $\text{CH}_3\text{NC}:\text{CH}_3\text{CN}$ ratio. The modelled abundance ratio of $\text{H}_2\text{CNC}:\text{H}_2\text{CCN}$ falls from 74% to 34% with the tested decrease in rate coefficients for Reactions 4 - 7, but the modelled $\text{H}_2\text{CNC}:\text{H}_2\text{CCN}$ ratio is in all cases higher than the observed $\text{H}_2\text{CNC}:\text{H}_2\text{CCN}$ ratio of $<2\%$ (see Section 2).

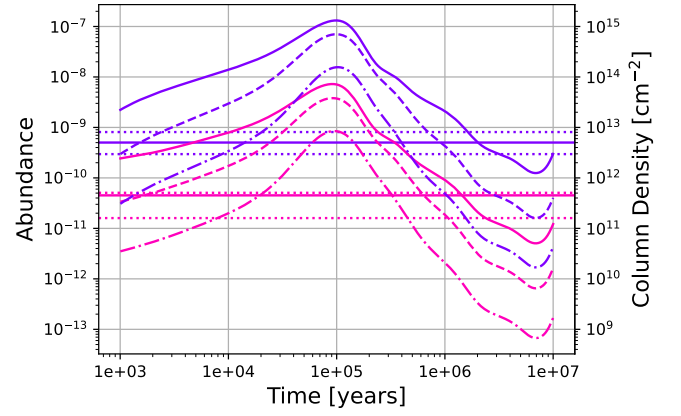


Figure 4. Modelled abundances/column densities of CH_3CN and CH_3NC over time. The solid curves represent the abundances modelled with standard reaction rate coefficients, the dashed curves represent the abundances modelled with rate coefficients corresponding to Reactions 4 - 7 lowered by one order of magnitude, and the dash-dotted curves represent the abundances modelled with these rate coefficients lowered by two orders of magnitude. The solid horizontal lines represent observed abundances/column densities and the dotted lines represent the uncertainties on these values. Purple represents CH_3CN and pink represents CH_3NC .

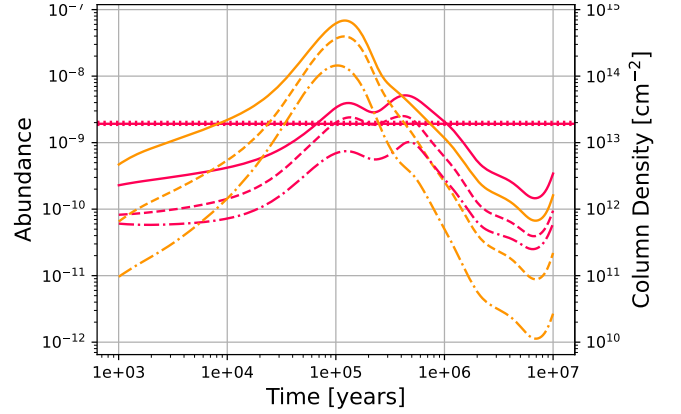


Figure 5. Modelled abundances/column densities of H_2CCN and H_2CNC over time. The solid curves represent the abundances modelled with standard reaction rate coefficients, the dashed curves represent the abundances modelled with rate coefficients corresponding to Reactions 4 - 7 lowered by one order of magnitude, and the dash-dotted curves represent the abundances modelled with these rate coefficients lowered by two orders of magnitude. The solid horizontal lines represent observed abundances/column densities and the dotted lines represent the uncertainties on these values. Red represents H_2CCN and orange represents H_2CNC .

4.2 Dissociative Recombination

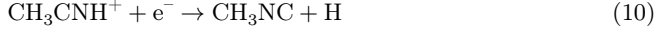
The molecules CH_3CN and CH_3NC are both predominantly formed by dissociative recombination of their protonated forms:



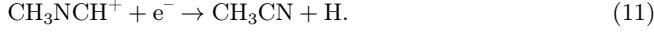
and



though about 15% of the modelled CH_3NC is formed from dissociative recombination of CH_3CNH^+ (Defrees et al. 1985, see later discussion of branching ratios), as the model also includes

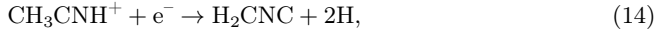
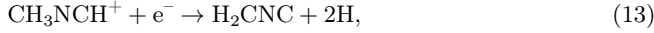
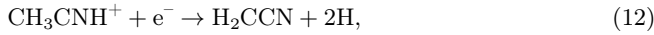


and

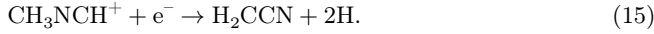


Like radiative association, dissociative recombination is a gas-phase process. Our modelled abundance of electrons is 1.2×10^{-8} at $\sim 5 \times 10^5$ years, in agreement with common estimates of the electron abundance of TMC-1 such as those of Lee et al. (1996).

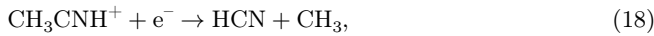
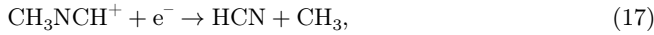
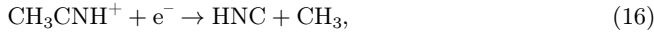
As with CH_3CN and CH_3NC , dissociative recombination reactions are also a key production route for the H_2CCN and H_2CNC radicals with one extra hydrogen-carbon bond breaking:



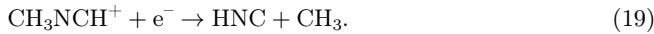
and



Another set of possibilities for dissociative recombination involves the cleaving of heavy atoms in the backbone, as in:



and



The isocyanide-to-cyanide ratios for the pairs of molecules considered here are set in part by the dissociative recombination reactions above. (Another major factor in setting this ratio is destruction; see Section 4.3). To determine the rate coefficients of Reactions 8 - 19, we rely on the insights gained from the research in Table 3.

To examine the relative abundances of the molecules of interest, we ran three models, "low isomerisation," "standard isomerisation," and "high isomerisation." The model with "standard isomerisation" uses exactly the information in Table 3, while "low isomerisation" only allows for half of the rearrangements of the "standard" model. For example, the rate coefficient for Reaction 10, which requires isomerisation, is cut in half. The "high isomerisation" model doubles the reaction rate coefficient for reactions that require isomerisation.

The results of these models are given in Table 4 and Figure 6. Increasing the branching ratio for a species does increase the abundance of that species as expected. The amount

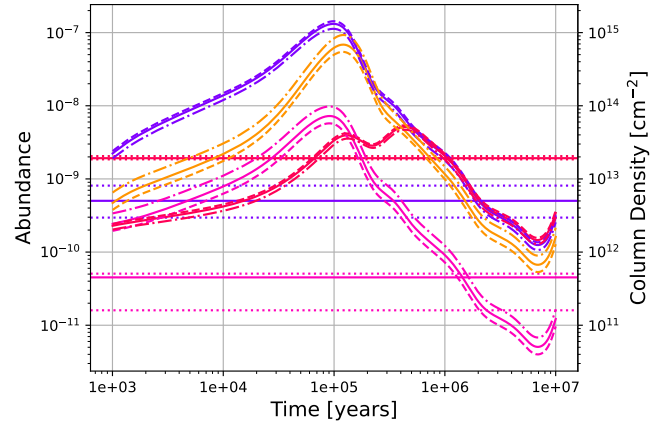


Figure 6. Abundances/column densities of species of interest from models of TMC-1 with differing branching ratios for dissociative recombination of CH_3CNH^+ and CH_3NCH^+ . The solid horizontal lines represent observed abundances/column densities and the dotted horizontal lines represent uncertainties on these values. The solid curve represents the model with "standard isomerisation." The dashed curves come from "low isomerisation" models and the dash-dotted curves come from "high isomerisation" models; see text for further model details. Purple represents CH_3CN , pink represents CH_3NC , red represents H_2CCN , and orange represents H_2CNC .

of the species of interest that comes from dissociative recombination does not change significantly in any of the models; it is the dominant production mechanism for CH_3CN , CH_3NC , H_2CCN , and H_2CNC , in all of our models and the case of 15% isomerization remains our standard. This is supported by the $\text{CH}_3\text{NC}:\text{CH}_3\text{CN}$ ratio, which is observed to be 5.9% and which is 3% for the "Low isomerisation" case, 5% for the "Standard isomerisation" case, and 8% for the "High isomerisation" case. The $\text{HNC}:\text{HCN}$ ratio is observed (Loison et al. 2014) to be close to or slightly less than one, which all three of these cases support.

4.3 Destruction Methods

One destructive reaction of particular interest is the destruction of CH_3NC by reaction with an H atom in the gas phase, explored in Section 3. Since hydrogen is highly abundant, an efficient reaction between these would likely be the dominant destruction process of CH_3NC . The abundance of H atoms is 3.1×10^{-5} in our models, on the same order of magnitude as the initial abundance of H atoms since most hydrogen is assumed to be in H_2 , which does not react with CH_3NC . Additionally, this reaction could set the $\text{CH}_3\text{CN}:\text{CH}_3\text{NC}$ ratio in a manner analogous to Reaction 2 for $\text{HNC}:\text{HNC}$. Willis et al. (2020) notes that varying the barrier height of this reaction alone changes the abundance of CH_3NC at late times dramatically in their models. As explained in Section 3, we investigated the reactions on this potential energy surface at the M062X/aug-cc-pVQZ level. The barrier height for the $\text{H}+\text{CH}_3\text{NC}$ reaction is found to be 2.191 kcal/mol (1102 K).

Using transition state theory and the parameters found with the methods described in Section 3 to calculate the $\text{H} + \text{CH}_3\text{NC}$ reaction rate coefficient in Table C1, we included this reaction in our *Nautilus* model of TMC-1; this method

Table 3. Findings of previous theoretical and experimental work used to determine appropriate rate coefficients for Reactions 8 - 19

Citation	Contribution(s)
Defrees et al. (1985)	15% of CH_3CNH^+ collision complexes isomerise to CH_3NCH^+ . Here, we assume 15% is the total of all reactions that require isomerisation from a specific precursor, CH_3CNH^+ or CH_3NCH^+ .
Plessis et al. (2010)	The branching ratio of a given product channel is not always correlated to its heat of formation. Rather than an energy-based weighting, we test multiple branching ratios for Reactions 8-19.
Vigren et al. (2008)	(1) One bond between heavy atoms of deuterated CH_3CNH^+ breaks in 35% of the dissociative recombinations (as in Reactions 16 - 19), whereas the C-C-N backbone is preserved 65% of the time (as in Reactions 8 - 15). (2) The total of the dissociative recombination rate coefficients (Reactions 8 - 19) is $\alpha = 8.13 \times 10^{-7} (T/300 \text{ K})^{-0.69} \text{ cm}^3 \text{ s}^{-1}$.
Loison et al. (2014)	If the C-C-N or C-N-C backbone is preserved, two hydrogen atoms dissociate 38% of the time (as in Reactions 12 - 15), and the remaining 62% of the time one hydrogen atom dissociates (as in Reactions 8 - 11).

Table 4. The abundances at $\sim 5 \times 10^5$ years. of molecules of interest for branching ratios on the dissociative recombination pathways for CH_3CNH^+ and CH_3NCH^+ . See text for description of models.

Molecule	Low Iso. Abundance	Standard Iso. Abundance	High Iso. Abundance
CH_3CN	5.50(-9)	5.05(-9)	4.35(-9)
CH_3NC	1.91(-10)	2.48(-10)	3.29(-10)
H_2CCN	5.16(-9)	4.92(-9)	4.51(-9)
H_2CNC	3.17(-9)	3.64(-9)	4.46(-9)
HCN	6.27(-8)	6.23(-8)	6.16(-8)
HNC	4.79(-8)	4.83(-8)	4.91(-8)

Notes. $a(b)$ refers to an abundance with respect to hydrogen of $a \times 10^b$.

is explained in Woon et al. (2021). In our model this reaction cannot explain the destruction of CH_3NC . Instead, CH_3NC is primarily destroyed by reaction with abundant ions. The rates of reaction between CH_3NC and the common interstellar ions H_3^+ , C^+ , HCO^+ , H_3O^+ , HOCO^+ , and H^+ were calculated following the method described by Woon & Herbst (2009); H_3^+ and C^+ were found to be the most effective in destroying CH_3NC in total reactive flux. The same method was used to calculate reaction rates between CH_3CN , H_2CCN , and H_2CNC and common interstellar ions and these reactions, too, were found to be the dominant destruction mechanism for these species in our models.

4.4 Temperature Effects

TMC-1 has extremely low rotational and excitation temperatures (T_{ex}), generally in the range 5–10 K. Models of TMC-1 typically assume $T_{gas} = T_{dust} = 10$ K (Hincelin et al. 2011; McGuire et al. 2020). The 10 K model produced here is the closest to physical conditions in TMC-1, but for comparison to other regions in the ISM we considered warmer models as well. The main production route for CH_3CN , CH_3NC , H_2CCN , and H_2CNC is dissociative recombination, which is a weakly temperature-dependent process (going as $T^{-0.5}$). The ion-neutral destruction routes also go as $T^{-0.5}$, but are slightly faster at higher temperatures because of the increased population of interstellar ions in warmer conditions and indeed, the models show a slight decrease in the abundances of the molecules at the highest temperature studied (30 K). At this temperature, the molecules and their destructive collision

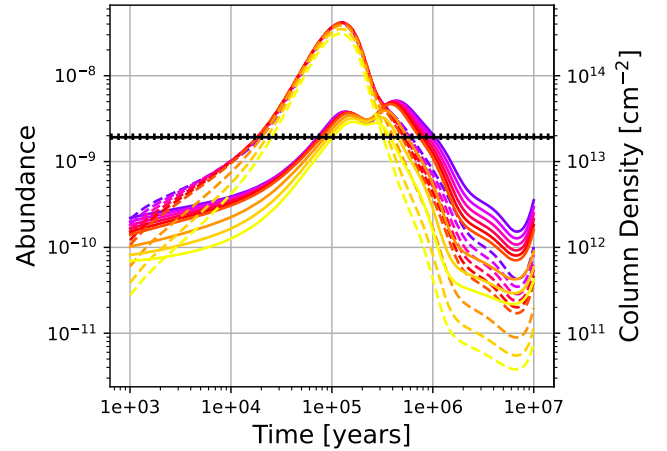


Figure 7. A comparison of the abundances of H_2CCN (solid) and H_2CNC (dashed) from models with temperatures of 10 K to 30 K, moving from purple to yellow as temperature increases. The solid black line represents the observed abundance/column density of H_2CCN , and the dotted black lines represent the uncertainty on this value.

partners collide more often and bring down the population of CH_3CN , CH_3NC , H_2CCN , and H_2CNC , though the effect is small, as can be seen in Figure 7 and Figure 8.

5 DISCUSSION

Other cyanides are found under TMC-1 conditions and are helpful in constraining the chemistry of the models. For example, the HNC/HCN ratio is known to be around unity to within a factor of two (Loison et al. 2014) which our models confirm; we find abundances under TMC-1 conditions of 6.2×10^{-8} and 4.8×10^{-8} with respect to hydrogen for HCN and HNC , respectively, at $\sim 5 \times 10^5$ years.

The overproduction of CH_3CN and CH_3NC , and to a lesser extent of H_2CCN and H_2CNC , in our models compared with their observed abundances could indicate the existence of an effective destruction mechanism in TMC-1 for these species not included in our models, or that the present rate of the production mechanism is overestimated. Our modelled $\text{CH}_3\text{NC}:\text{CH}_3\text{CN}$ abundance ratio, 5%, closely reproduces the observed column density ratio, $5.9_{-3.9}^{+11.2}\%$, within error bounds. Calcutt et al. (2018) find an opposite result in

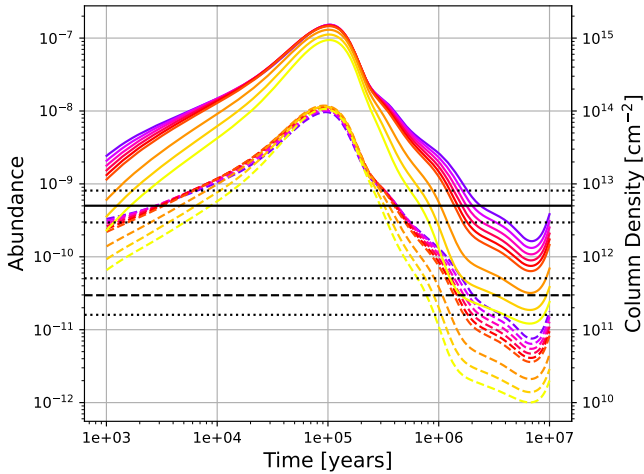


Figure 8. A comparison of the abundances of CH_3CN (solid) and CH_3NC (dashed) from models with temperatures of 10 K to 30 K, moving from purple to yellow as temperature increases. Observed abundances/column densities are represented in black, and the dotted black lines represent uncertainties on these values.

modelling the solar-type protostars IRAS 16293-2422 A and B, for which modelled isocyanide-to-cyanide ratios are higher than that which is observed. In both models, an effective destruction mechanism that differentiates between CH_3CN and CH_3NC would help close the gap between modelled and observed abundances. One particularly interesting set of reactions along these lines is that studied by [Nguyen et al. \(2019\)](#), who find that on grain surfaces, CH_3NC has a significantly higher barrier to successive hydrogenation into CH_3NHCH_3 than CH_3CN does to $\text{CH}_3\text{CH}_2\text{NH}_2$. An additional mechanism for study might be dissociative electron attachment, whereby an electron attaches to a neutral molecule, forming an anion that dissociates into two or more fragments. [Luxford & Nag \(2021\)](#) find that the dissociative electron attachment pathways for CH_3CN and CH_3NC , while largely similar, diverge such that CH_3CN more readily splits into an H atom and H_2CCN^- than CH_3NC does an H atom and H_2CNC^- . These reaction pathways remain to be studied in chemical kinetic models to the best of our knowledge.

6 CONCLUSIONS

The molecules CH_3NC and H_2CCN are detected in TMC-1 using hyperfine-resolved rotational emission lines matched to a spectral line survey from the GOTHAM large project on the Green Bank Telescope. This is the first time CH_3NC has been discovered in a low-temperature environment.

Though the backbone is only one one carbon longer than HCN and HNC, the observed ratio of $\text{CH}_3\text{NC}:\text{CH}_3\text{CN}$ is about 6%, compared to the near parity found between HCN and HNC. The modelled ratio of $\text{H}_2\text{CNC}:\text{H}_2\text{CCN}$ is highly time dependent. Though many reaction pathways were investigated (see Table C1), the dominant production route for CH_3CN , CH_3NC , H_2CCN , and H_2CNC in our models is the dissociative recombination of CH_3CNH^+ and CH_3NCH^+ , and the dominant destruction route for these four molecules

in our models is reaction with abundant ions such as H^+ , H_3^+ , and C^+ . Why isocyanide-to-cyanide ratios are so different remains to be seen, and investigations as to the observed abundance of H_2CNC (as yet undetected) would be helpful in constraining gas-phase chemistry in TMC-1, which remains a fascinating area for inquiry.

ACKNOWLEDGEMENTS

We thank H. S. P. Müller for providing the spectroscopic information about H_2CCN and helping interpret the hyperfine quantum numbers. E. H. thanks the National Science Foundation for support of his program in astrochemistry via grant AST 19-06489. B. A. M. and C.X. gratefully acknowledge support of NSF grant AST-2205126. The National Radio Astronomy Observatory is a facility of the National Science Foundation operated under cooperative agreement by Associated Universities, Inc. The Green Bank Observatory is a facility of the National Science Foundation operated under cooperative agreement by Associated Universities, Inc.

DATA AVAILABILITY

The data underlying the modeling of this article may be found in the Kinetic Database for Astrochemistry (KIDA) network (<https://astrophy.u-bordeaux.fr>) and in the article. The project codes for the GBT observations include AGBT17A-164, AGBT17A-434, AGBT18A-333, AGBT18B-007, AGBT19B-047, AGBT20A-516, AGBT21A-414, and AGBT21B-210. The datasets are available in the Green Bank Telescope archive (<https://archive.nrao.edu/archive/advquery.jsp>; PI: B.A.M.). A user manual for their reduction and analysis is also available (<https://greenbankobservatory.org/science/gbt-observers/visitor-facilities-policies/data-reduction-gbt-using-idl/>).

REFERENCES

- Anicich V. G., Sen A. D., McEwan M. J., Smith S. C., 1994, *J. Chem. Phys.*, **100**, 5696
- Anicich V. G., Sen A. D., Huntress Wesley T. J., McEwan M. J., 1995, *J. Chem. Phys.*, **102**, 3256
- Calcutt H., et al., 2018, *A&A*, **617**, A95
- Cernicharo J., Kahane C., Guelin M., Gomez-Gonzalez J., 1988, *A&A*, **189**, L1
- Defrees D. J., McLean A. D., Herbst E., 1985, *ApJ*, **293**, 236
- Dobashi K., Shimoikura T., Nakamura F., Kameno S., Mizuno I., Taniguchi K., 2018, *ApJ*, **864**, 82
- Frisch M. J., et al., 2016, Gaussian-16 Revision C.01
- Ginard D., et al., 2012, *A&A*, **543**, A27
- Gonzalez C., Schlegel H. B., 1989, *J. Chem. Phys.*, **90**, 2154
- Gonzalez C., Schlegel H. B., 1990, *The Journal of Physical Chemistry*, **94**, 5523
- Graninger D. M., Herbst E., Öberg K. I., Vasyunin A. I., 2014, *ApJ*, **787**, 74
- Graninger D., Öberg K. I., Qi C., Kastner J., 2015, *ApJ*, **807**, L15
- Gratier P., Pety J., Guzmán V., Gerin M., Goicoechea J. R., Roueff E., Faure A., 2013, *A&A*, **557**, A101
- Gratier P., Majumdar L., Ohishi M., Roueff E., Loison J. C., Hickson K. M., Wakelam V., 2016, *ApJS*, **225**, 25
- Hasegawa T. I., Herbst E., Leung C. M., 1992, *ApJS*, **82**, 167

- Hincelin U., Wakelam V., Hersant F., Guilloteau S., Loison J.-C., Honvault P., Troe J., 2011, *Astronomy and Astrophysics*, 530
- Hirao T., Ozeki H., Saito S., Yamamoto S., 2007, *The Journal of Chemical Physics*, 127, 134312
- Irvine W. M., Schloerb F. P., 1984, *ApJ*, 282, 516
- Knizia G., Adler T. B., Werner H.-J., 2009, *J. Chem. Phys.*, 130, 054104
- Kukolich S. G., 1972, *J. Chem. Phys.*, 57, 869
- Kukolich S. G., Ruben D. J., Wang J. H. S., Williams J. R., 1973, *J. Chem. Phys.*, 58, 3155
- Lee H. H., Bettens R. P. A., Herbst E., 1996, *A&AS*, 119, 111
- Lee K. L. K., et al., 2021, *ApJ*, 908, L11
- Loison J.-C., Wakelam V., Hickson K. M., 2014, *MNRAS*, 443, 398
- Loomis R. A., et al., 2021, *Nature Astronomy*, 5, 188
- Luxford T. F. M., Nag P., 2021, *European Physical Journal D*, 75, 270
- McGuire B. A., 2022, *ApJS*, 259, 30
- McGuire B. A., et al., 2020, *ApJ*, 900, L10
- McGuire B. A., et al., 2021, *Science*, 371, 1265
- Müller H. S. P., Schlöder F., Stutzki J., Winnewisser G., 2005, *Journal of Molecular Structure*, 742, 215
- Nelson R., of Standards U. S. N. B., Lide D., Maryott A., 1967, Selected Values of Electric Dipole Moments for Molecules in the Gas Phase. NSRDS-NBS, U.S. National Bureau of Standards, <https://books.google.com/books?id=iZAuAAAATAAJ>
- Nguyen T., et al., 2019, *A&A*, 628, A15
- Ozeki H., Hirao T., Saito S., Yamamoto S., 2004, *ApJ*, 617, 680
- Peterson K. A., Adler T. B., Werner H.-J., 2008, *J. Chem. Phys.*, 128, 084102
- Peverati R., Truhlar D. G., 2014, *Philosophical Transactions of the Royal Society of London Series A*, 372, 20120476
- Plessis S., Carrasco N., Pernot P., 2010, *J. Chem. Phys.*, 133, 134110
- Pliva J., Le L., Johns J., Lu Z., Bernheim R., 1995, *Journal of Molecular Spectroscopy*, 173, 423
- Pracna P., Urban J., Votava O., Meltzerova Z., Urban S., Horne- man V.-M., Drouin B. J., 2011, *The Journal of Physical Chemistry A*, 115, 1063
- Purcell C. R., et al., 2006, *MNRAS*, 367, 553
- Remijan A. J., Hollis J. M., Lovas F. J., Plusquellic D. F., Jewell P. R., 2005, *ApJ*, 632, 333
- Ruaud M., Wakelam V., Hersant F., 2016, *MNRAS*, 459, 3756
- Schilke P., Walmsley C. M., Pineau Des Forets G., Roueff E., Flower D. R., Guilloteau S., 1992, *A&A*, 256, 595
- Sita M. L., et al., 2022, arXiv e-prints, p. arXiv:2209.06851
- Snyder L. E., Buhl D., 1971, *ApJ*, 163, L47
- Snyder L. E., Buhl D., 1972, *Annals of the New York Academy of Sciences*, 194, 17
- Vigren E., et al., 2008, *Physical Chemistry Chemical Physics (Incorporating Faraday Transactions)*, 10, 4014
- Wakelam V., Herbst E., 2008, *ApJ*, 680, 371
- Werner H., Knowles P., Knizia G., Manby F., Schütz M., 2012, *Wiley Interdisciplinary Reviews: Computational Molecular Science*, 2, 242
- Werner H.-J., et al., 2020, *J. Chem. Phys.*, 152, 144107
- Willis E. R., Garrod R. T., Belloche A., Müller H. S. P., Barger C. J., Bonfand M., Menten K. M., 2020, *Astronomy & Astrophysics*, 636, 1
- Woon D. E., Herbst E., 2009, *ApJS*, 185, 273
- Woon D. E., Maffucci D. M., Herbst E., 2021, *Icarus*, 354, 114051
- Xue C., et al., 2020, *ApJ*, 900, L9
- Zhao Y., Truhlar D., 2008, *Theoretical Chemistry Accounts*, pp 215–241

APPENDIX A: OBSERVED HYPERFINE TRANSITIONS

Table A1 summarizes the spectroscopic properties of the hyperfine components for CH₃NC, CH₃CN, H₂CCN, and H₂CNC as discussed in Section 2. The data of H₂CCN and CH₃CN are taken from the CDMS catalog (Müller et al. 2005); the entry was based on Ozeki et al. (2004) for H₂CCN and Kukolich et al. (1973) for CH₃CN respectively. For four of the H₂CCN transitions, we use the calculated frequencies rather than the measured values reported in Ozeki et al. (2004). This is due to the fact that the calculated frequencies match the astronomical observations. The entries for H₂CNC were calculated using the spectroscopic constants derived from the laboratory rest frequencies measured by Hirao et al. (2007). The fine and hyperfine structure are similar to that of H₂CCN, with well-resolved magnetic dipole and electric quadrupole splittings from the electronic and nuclear spins. The dipole moment of H₂CNC was taken to be $\mu = 3.5 \pm 0.5$ D to derive the upper bound to its column density.

The hyperfine catalog for CH₃NC is generated with the rotational and centrifugal distortion constants from Pracna et al. (2011) and Pliva et al. (1995) and the ¹⁴N quadrupole coupling constants from Kukolich (1972). The latter study also reports the ¹H magnetic hyperfine constants, but the associated structure is much smaller than the observation resolution and therefore neglected here. We use the electric dipole moment of 3.85 D for CH₃NC (Nelson et al. 1967).

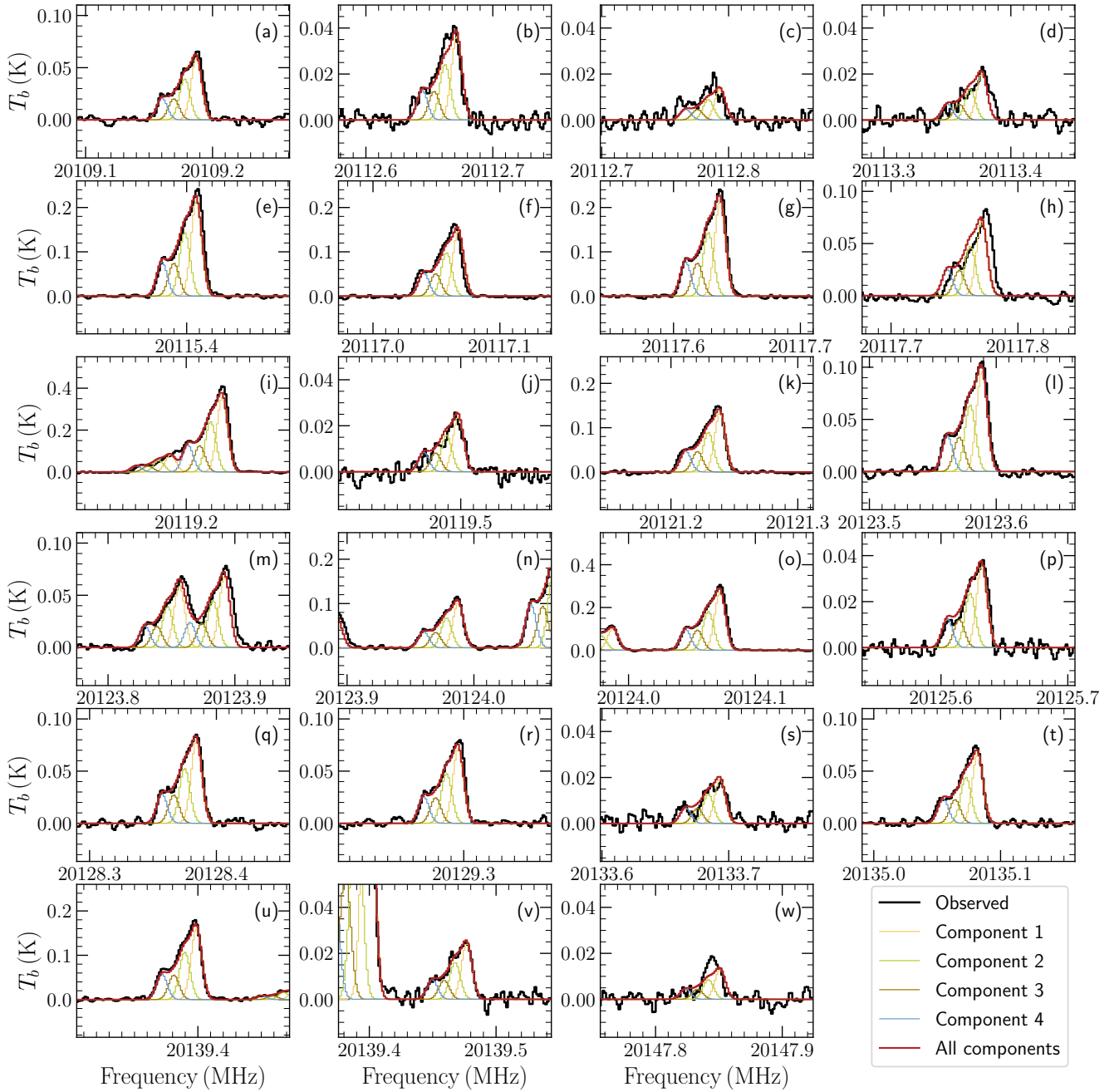


Figure A1. Individual line detection of $\text{H}_2\text{CCN } 1_{0,1} - 0_{0,0}$ transitions in the GOTHAM DR4 data. Each panel provides a window context of 2.5 km s^{-1} , and the alphabetical label in the top-right corner corresponds to that in the last column in Table A1. are in the top right corner. The observed spectra are displayed in black while the best-fitting model to the data, including all velocity components, is overlaid in red. Simulated spectra of the individual velocity components are shown in: yellow (5.63 km s^{-1}), green (5.77 km s^{-1}), brown (5.90 km s^{-1}), and blue (6.04 km s^{-1}). See Table B1.

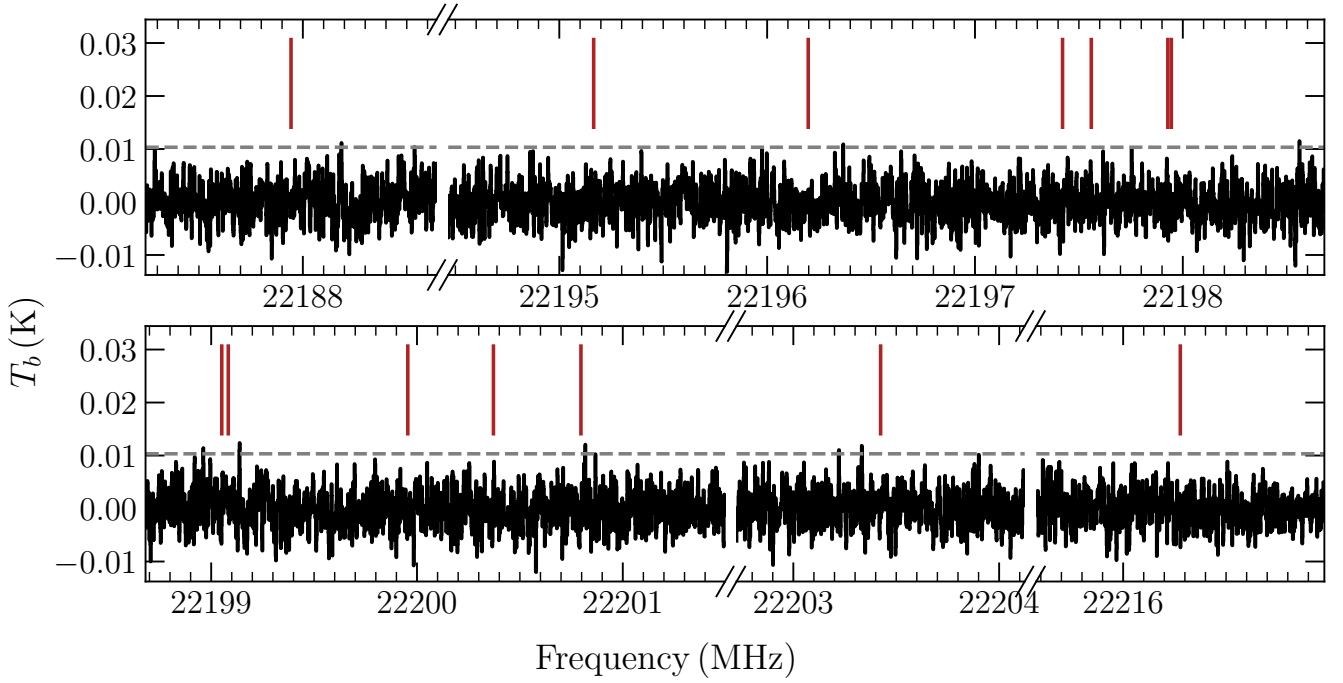


Figure A2. H_2CNC $1_{0,1} - 0_{0,0}$ transitions in the GOTHAM DR4 data. 3σ noise level are indicated by grey dashed lines. 14 hyperfine components are marked with red vertical lines with an assumed systemic velocity of TMC-1, $V_{\text{sys}} = 5.8 \text{ km s}^{-1}$. See Table A1 for spectroscopic details.

Table A1. Spectroscopic Properties of Observed Transitions

Species	$N'_{Ka',Kc'} - N''_{Ka'',Kc''}$ *	Transitions		Rest Frequency (MHz)	E_{up} (K)	$\log_{10} \frac{A_{ul}}{s^{-1}}$	$S_{ij} \mu^2$ (D ²)	Observed Spectra
		$F'_1 - F''_1$ †	$F' - F''$ †					
CH ₃ NC	$1_0 - 0_0$	0 - 1		20105.5078(92)	0.96	-6.3213	5.04	Fig 1
		2 - 1		20105.7281(92)		-6.3214	25.22	
		1 - 1		20105.8749(92)		-6.3213	15.13	
CH ₃ CN	$1_0 - 0_0$	1 - 1		18396.7253(10)	0.88	-6.4300	30.77	Fig 2
		2 - 1		18397.9970(10)		-6.4300	51.27	
		0 - 1		18399.8924(10)		-6.4300	10.25	
H ₂ CCN	$1_{0,1} - 0_{0,0}$	2.5 - 1.5	2.5 - 2.5	20109.5659(30)	0.97	-7.0852	5.21	Fig A1(a)
		2.5 - 1.5	1.5 - 1.5	20113.0502(30) [‡]		-7.1205	3.20	Fig A1(b)
		1.5 - 1.5	1.5 - 2.5	20113.1719(30)		-7.5564	1.17	Fig A1(c)
		0.5 - 0.5	0.5 - 0.5	20113.7558(30)		-7.0809	1.75	Fig A1(d)
		1.5 - 1.5	2.5 - 2.5	20115.7864(30)		-6.5170	19.26	Fig A1(e)
		2.5 - 1.5	1.5 - 0.5	20117.4459(30)		-6.5088	13.08	Fig A1(f)
		2.5 - 1.5	2.5 - 1.5	20118.0154(30)		-6.5162	19.29	Fig A1(g)
		0.5 - 0.5	0.5 - 1.5	20118.1503(30)		-6.5277	6.26	Fig A1(h)
		0.5 - 0.5	1.5 - 0.5	20119.5664(30)		-6.7651	7.25	Fig A1(i)
		2.5 - 1.5	3.5 - 2.5	20119.6072(30)		-6.4122	32.66	Fig A1(j)
		1.5 - 1.5	0.5 - 1.5	20119.8768(30)		-7.0019	2.10	Fig A1(k)
		1.5 - 1.5	1.5 - 1.5	20121.6175(30)		-6.5485	11.93	Fig A1(l)
		0.5 - 0.5	1.5 - 1.5	20123.9675(30)		-6.6957	8.50	Fig A1(m)
		1.5 - 1.5	2.5 - 1.5	20124.2351(30)		-7.0867	5.18	Fig A1(n)
		1.5 - 1.5	0.5 - 0.5	20124.2707(30) [‡]		-6.5484	5.96	Fig A1(o)
		1.5 - 0.5	1.5 - 0.5	20124.3665(30)		-6.6711	8.99	Fig A1(p)
		1.5 - 0.5	2.5 - 1.5	20124.4510(30)		-6.4132	24.43	Fig A1(q)
		1.5 - 1.5	1.5 - 0.5	20126.0111(30)		-7.1296	3.13	Fig A1(r)
		1.5 - 0.5	1.5 - 1.5	20128.7632(30)		-6.7809	6.98	Fig A1(s)
		1.5 - 0.5	0.5 - 0.5	20129.6746(30)		-6.5231	6.32	Fig A1(t)
		1.5 - 0.5	0.5 - 1.5	20134.0722(30)		-7.0963	1.69	Fig A1(u)
0.5 - 1.5	0.5 - 1.5	20135.4610(30) [‡]	-6.5573	5.83	Fig A1(v)			
0.5 - 1.5	1.5 - 2.5	20139.7780(30)	-6.4697	14.27	Fig A1(w)			
H ₂ CNC	$1_{0,1} - 0_{0,0}$	0.5 - 1.5	0.5 - 0.5	20139.8560(30) [‡]	-6.9973	2.12	Fig A1(x)	
		0.5 - 1.5	1.5 - 1.5	20148.2302(30)	-7.5713	1.13	Fig A1(y)	
		1.5 - 1.5	1.5 - 1.5	22188.3724(16)	-7.9035	0.39	Fig A2	
		1.5 - 1.5	2.5 - 2.5	22195.5948(12)	-7.3837	1.95		
		1.5 - 1.5	0.5 - 1.5	22196.6271(13)	-7.5524	0.44		
		0.5 - 0.5	0.5 - 1.5	22197.8508(11)	-7.3813	0.65		
		2.5 - 1.5	2.5 - 1.5	22197.9890(10)	-7.3835	1.95		
		2.5 - 1.5	3.5 - 2.5	22198.3573(10)	-7.3722	2.67		
		2.5 - 1.5	1.5 - 0.5	22198.3741(9)	-7.3897	1.28		
		1.5 - 0.5	1.5 - 1.5	22199.4809(10)	-7.3744	1.33		
		1.5 - 0.5	0.5 - 0.5	22199.5125(8)	-7.3787	0.66		
		0.5 - 0.5	1.5 - 0.5	22200.3849(13)	-7.3764	1.32		
		1.5 - 0.5	2.5 - 1.5	22200.8010(7)	-7.3722	2.00		
		1.5 - 1.5	1.5 - 2.5	22201.2262(11)	-7.5457	0.89		
		0.5 - 1.5	1.5 - 1.5	22203.8537(14)	-7.5271	0.93		
0.5 - 1.5	1.5 - 2.5	22216.7075(16)	-7.9182	0.38				

Notes. (*) $J'_{K'c'} - J''_{K''c''}$ for CH₃CN and CH₃NC. (†) The ortho H₂CCN ($K_a = 0$) species employs the coupling scheme of $J = N + S$, $F_1 = J + I_H$, and $F = F_1 + I_N$ whereas CH₃CN and CH₃NC employ the coupling scheme of $F_1 = J + I_N$, and $F = F_1 + I_H$, where I_N is the nitrogen spin and I_H is the total hydrogen spin. (‡) Calculated frequencies reported in Ozeki et al. (2004) are adapted here to better fit the GOTHAM observations.

[h]

Table B1. H_2CCN best-fitting parameters from the MCMC analysis

Component	v_{lsr} (km s ⁻¹)	Size ($''$)	N_T (10^{13} cm ⁻²)	T_{ex} (K)	ΔV (km s ⁻¹)
C1	$5.633^{+0.002}_{-0.002}$	250^{+104}_{-108}	$0.82^{+0.04}_{-0.02}$		
C2	$5.771^{+0.004}_{-0.004}$	228^{+122}_{-114}	$0.54^{+0.04}_{-0.02}$	[6.7]	$0.148^{+0.002}_{-0.002}$
C3	$5.898^{+0.005}_{-0.005}$	222^{+124}_{-124}	$0.28^{+0.03}_{-0.02}$		
C4	$6.039^{+0.002}_{-0.002}$	233^{+117}_{-119}	$0.29^{+0.02}_{-0.01}$		
N_T (Total)		$1.92^{+0.13}_{-0.07} \times 10^{13}$ cm ⁻²			

Notes. – Similar to Table 1.

APPENDIX B: MCMC FITTING RESULTS

The radical H_2CCN has been previously detected in TMC-1 with Nobeyama 45 m observations (Gratier et al. 2016), which reported its N_T to be $3.80^{+2.81}_{-2.06} \times 10^{13}$ cm⁻² with a T_{ex} of 3.46 K. In order to achieve self-consistency, an identical analysis to that for CH_3NC and CH_3CN was carried out for H_2CCN with the GOTHAM observations. The resulting parameters are given in Table B1. A total N_T of $1.92^{+0.13}_{-0.07} \times 10^{13}$ cm⁻² with a fixed T_{ex} of 6.7 K is determined for H_2CCN .

A corner plot of the parameter covariances and their distribution for the MCMC fit is shown in Figure B1 for CH_3NC , Figure B2 for CH_3CN , and Figure B3 for H_2CCN . Worth noting is the strong covariance between the column density and the source size for each component. Limited by the frequency coverage of the detected lines, the source sizes of molecular emission are poorly constrained, which leads to the uncertainty in the total column density.

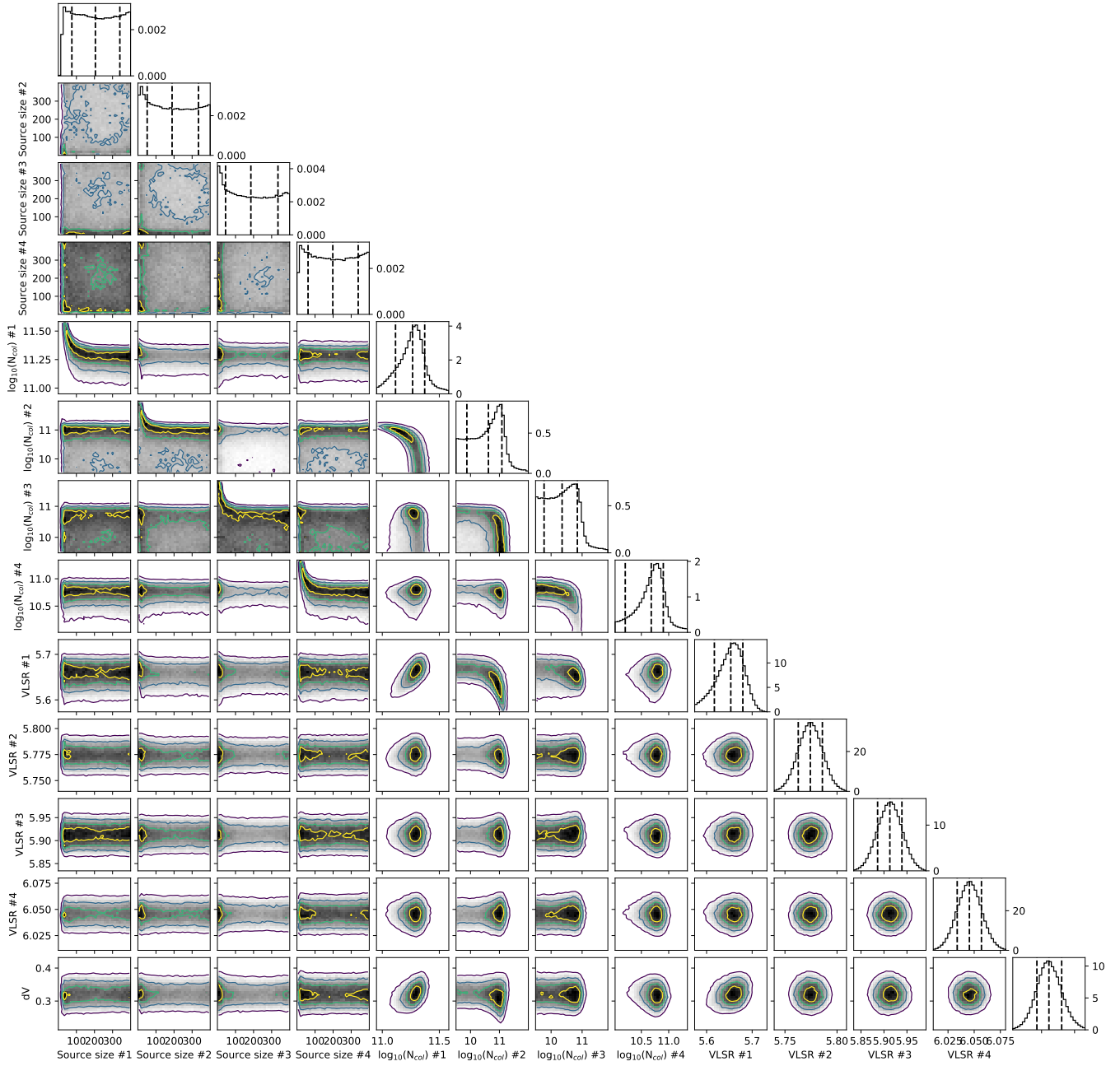


Figure B1. Parameter covariances and marginalized posterior distributions for the CH_3NC MCMC fit. 16^{th} , 50^{th} , and 84^{th} confidence intervals (corresponding to ± 1 sigma for a Gaussian posterior distribution) are shown as vertical lines.

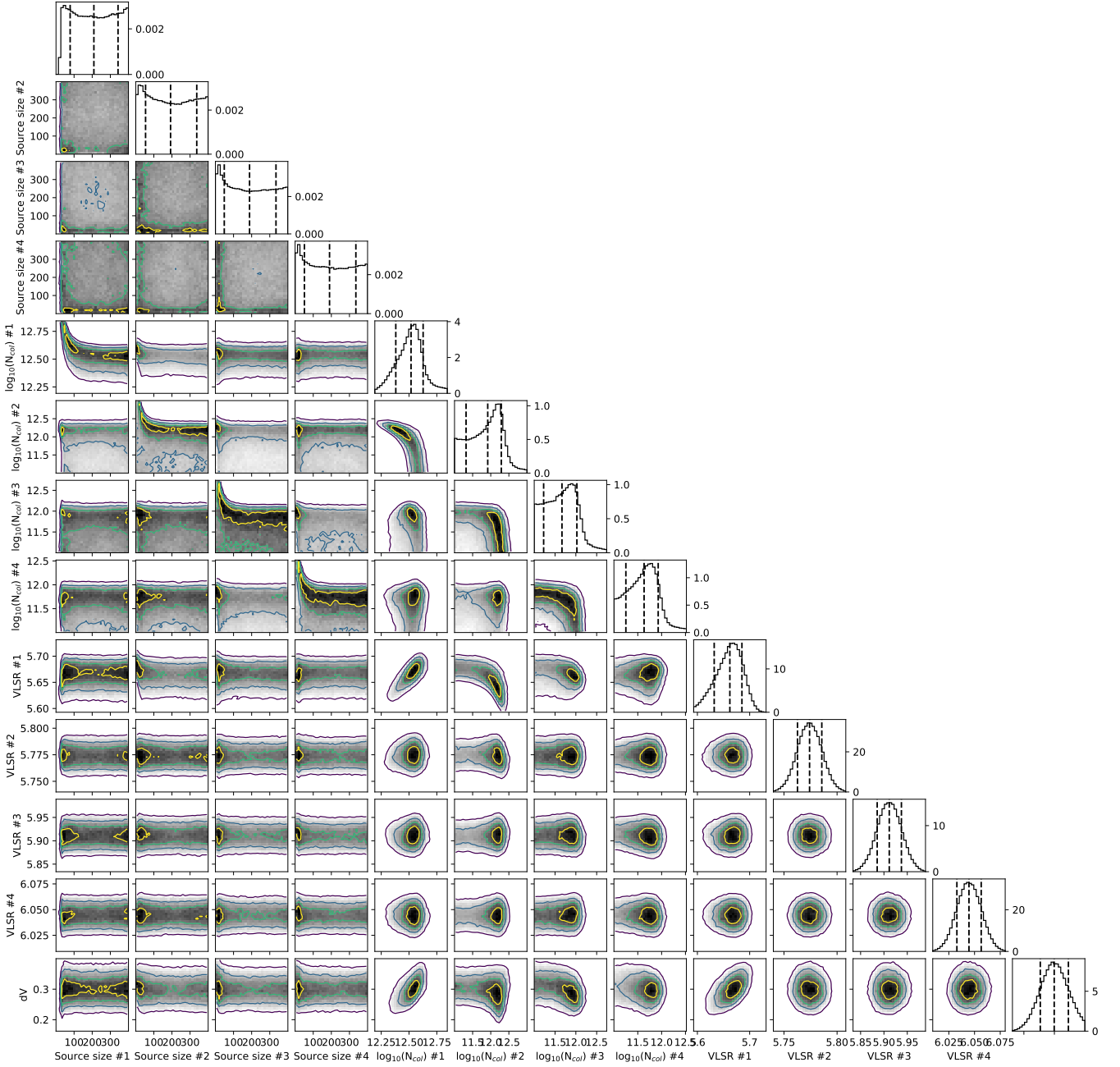


Figure B2. Parameter covariances and marginalized posterior distributions for the CH_3CN MCMC fit. 16th, 50th, and 84th confidence intervals (corresponding to ± 1 sigma for a Gaussian posterior distribution) are shown as vertical lines.

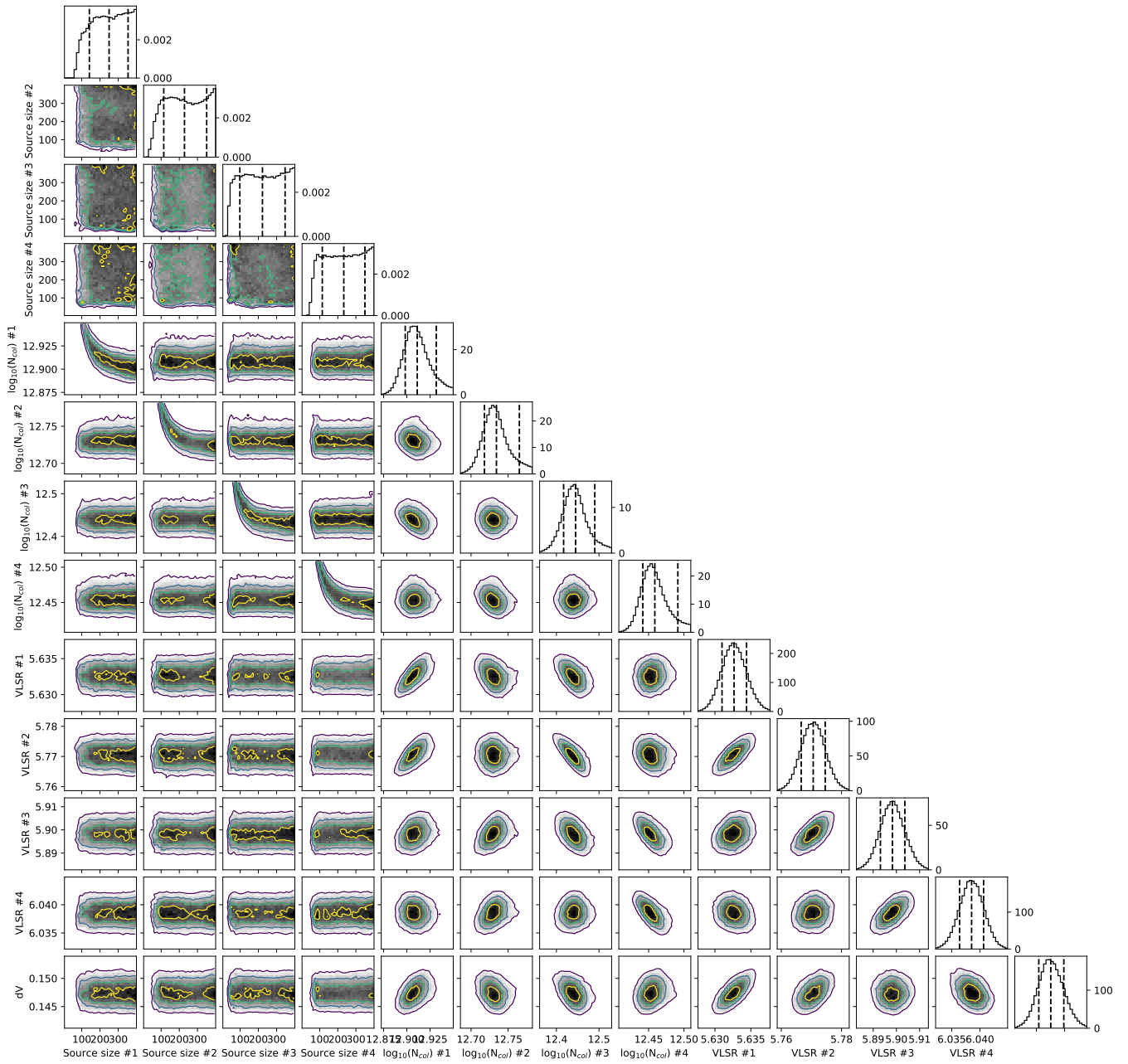


Figure B3. Parameter covariances and marginalized posterior distributions for the H_2CCN MCMC fit. 16^{th} , 50^{th} , and 84^{th} confidence intervals (corresponding to ± 1 sigma for a Gaussian posterior distribution) are shown as vertical lines.

APPENDIX C: REACTIONS ADDED TO NAUTILUS

Table C1 below gives the gas-phase and then the grain-surface reactions added to our model. Adsorption, desorption, bulk mixing, and grain-surface photodestruction reactions are also included for each new species of interest and precursor but are not listed. The rates r_{AB} of the grain-surface reactions are given by $r_{AB} = \kappa_{AB}(r_{\text{diff,A}} + r_{\text{diff,B}})$ where $r_{\text{diff,X}}$ is the rate of diffusion of the grain-surface reactant, and κ_{AB} is related to the activation energy given in the table as in Hasegawa et al. (1992).

Table C1: Reactions added to Nautilus.

Gas-Phase Reaction	Rate*	Units	Reference
$H + CH_3NC \rightarrow HCN + CH_3$	$3.42 \times 10^{-14} (T/300K)^{-2.19} e^{-1102K/T}$	$\text{cm}^3 \text{s}^{-1}$	<i>a</i>
$CH_3CNH^+ + e^- \rightarrow H + CH_3NC$	$4.55 \times 10^{-8} (T/300K)^{-0.69}$	$\text{cm}^3 \text{s}^{-1}$	<i>a</i> ; see Fig. 6
$CH_3NCH^+ + e^- \rightarrow H + H + H_2CNC$	$1.71 \times 10^{-7} (T/300K)^{-0.69}$	$\text{cm}^3 \text{s}^{-1}$	<i>a</i> ; see Fig. 6
$CH_3NCH^+ + e^- \rightarrow H + H + H_2CCN$	$3.02 \times 10^{-8} (T/300K)^{-0.69}$	$\text{cm}^3 \text{s}^{-1}$	<i>a</i> ; see Fig. 6
$CH_3NCH^+ + e^- \rightarrow H + CH_3CN$	$4.98 \times 10^{-8} (T/300K)^{-0.69}$	$\text{cm}^3 \text{s}^{-1}$	<i>a</i> ; see Fig. 6
$CH_3NCH^+ + e^- \rightarrow H + CH_3NC$	$2.78 \times 10^{-7} (T/300K)^{-0.69}$	$\text{cm}^3 \text{s}^{-1}$	<i>a</i> ; see Fig. 6
$CH_3NCH^+ + e^- \rightarrow HNC + CH_3$	$2.42 \times 10^{-7} (T/300K)^{-0.69}$	$\text{cm}^3 \text{s}^{-1}$	<i>a</i> ; see Fig. 6
$CH_3NCH^+ + e^- \rightarrow HCN + CH_3$	$4.27 \times 10^{-8} (T/300K)^{-0.69}$	$\text{cm}^3 \text{s}^{-1}$	<i>a</i> ; see Fig. 6
$CH_2NC^+ + e^- \rightarrow CH + HCN$	$2.00 \times 10^{-7} (T/300K)^{-0.5}$	$\text{cm}^3 \text{s}^{-1}$	<i>b</i>
$CH_2NC^+ + e^- \rightarrow CN + CH_2$	$2.00 \times 10^{-7} (T/300K)^{-0.5}$	$\text{cm}^3 \text{s}^{-1}$	<i>b</i>
$CH_2NC^+ + e^- \rightarrow H + H + CCN$	$2.00 \times 10^{-7} (T/300K)^{-0.5}$	$\text{cm}^3 \text{s}^{-1}$	<i>b</i>
$CH_3NC^+ + e^- \rightarrow H + H_2 + CCN$	$2.00 \times 10^{-7} (T/300K)^{-0.5}$	$\text{cm}^3 \text{s}^{-1}$	<i>b</i>
$CH_3NC^+ + e^- \rightarrow CH_2 + HCN$	$1.00 \times 10^{-7} (T/300K)^{-0.5}$	$\text{cm}^3 \text{s}^{-1}$	<i>b</i>
$CH_3NC^+ + e^- \rightarrow CN + CH_3$	$1.00 \times 10^{-7} (T/300K)^{-0.5}$	$\text{cm}^3 \text{s}^{-1}$	<i>b</i>
$CH_3NC^+ + e^- \rightarrow H + H_2CNC$	$2.00 \times 10^{-7} (T/300K)^{-0.5}$	$\text{cm}^3 \text{s}^{-1}$	<i>b</i>
$CH_3NC + CRP \rightarrow CN + CH_3$	$4.76 \times 10^3 \zeta$	s^{-1}	<i>b</i>
$CH_3NC + CRP \rightarrow CH_3NC^+ + e^-$	$2.24 \times 10^3 \zeta$	s^{-1}	<i>b</i>
$CH_3NC + \text{Photon} \rightarrow CN + CH_3$	$2.50 \times 10^{-9} e^{-2.58A_v}$	s^{-1}	<i>b</i>
$CH_3NC + \text{Photon} \rightarrow CH_3NC^+ + e^-$	$6.20 \times 10^{-10} e^{-3.11A_v}$	s^{-1}	<i>b</i>
$H_2CNC + \text{Photon} \rightarrow CH_2NC^+ + e^-$	$2.65 \times 10^{-10} e^{-3.11A_v}$	s^{-1}	<i>b</i>
$H_2CCN + He^+ \rightarrow He + CH_2^+ + CN$	$2.57 \times 10^{-9} [0.62 + 2.77(300K/T)^{0.5}]$	$\text{cm}^3 \text{s}^{-1}$	<i>a,c</i>
$H_2CCN + H_3^+ \rightarrow H_2 + CH_3CN^+$	$4.90 \times 10^{-9} [0.62 + 2.77(300K/T)^{0.5}]$	$\text{cm}^3 \text{s}^{-1}$	<i>a,c</i>
$H_2CCN + C^+ \rightarrow C + CH_2CN^+$	$1.61 \times 10^{-9} [0.62 + 2.77(300K/T)^{0.5}]$	$\text{cm}^3 \text{s}^{-1}$	<i>a,c</i>
$H_2CCN + HCO^+ \rightarrow CO + CH_3CN^+$	$1.19 \times 10^{-9} [0.62 + 2.77(300K/T)^{0.5}]$	$\text{cm}^3 \text{s}^{-1}$	<i>a,c</i>
$H_2CCN + H_3O^+ \rightarrow H_2O + CH_3CN^+$	$1.36 \times 10^{-9} [0.62 + 2.77(300K/T)^{0.5}]$	$\text{cm}^3 \text{s}^{-1}$	<i>a,c</i>
$H_2CCN + HOCO^+ \rightarrow CO_2 + CH_3CN^+$	$1.06 \times 10^{-9} [0.62 + 2.77(300K/T)^{0.5}]$	$\text{cm}^3 \text{s}^{-1}$	<i>a,c</i>
$H_2CCN + H^+ \rightarrow H + CH_2CN^+$	$4.94 \times 10^{-9} [0.62 + 2.77(300K/T)^{0.5}]$	$\text{cm}^3 \text{s}^{-1}$	<i>a,c</i>
$H_2CNC + He^+ \rightarrow He + CH_2^+ + CN$	$2.57 \times 10^{-9} [0.62 + 2.77(300K/T)^{0.5}]$	$\text{cm}^3 \text{s}^{-1}$	<i>b</i>
$H_2CNC + H_3^+ \rightarrow H_2 + CH_3NC^+$	$4.90 \times 10^{-9} [0.62 + 2.77(300K/T)^{0.5}]$	$\text{cm}^3 \text{s}^{-1}$	<i>b</i>
$H_2CNC + C^+ \rightarrow C + CH_2NC^+$	$1.61 \times 10^{-9} [0.62 + 2.77(300K/T)^{0.5}]$	$\text{cm}^3 \text{s}^{-1}$	<i>b</i>
$H_2CNC + HCO^+ \rightarrow CO + CH_3NC^+$	$1.19 \times 10^{-9} [0.62 + 2.77(300K/T)^{0.5}]$	$\text{cm}^3 \text{s}^{-1}$	<i>b</i>
$H_2CNC + H_3O^+ \rightarrow H_2O + CH_3NC^+$	$1.36 \times 10^{-9} [0.62 + 2.77(300K/T)^{0.5}]$	$\text{cm}^3 \text{s}^{-1}$	<i>b</i>
$H_2CNC + HOCO^+ \rightarrow CO_2 + CH_3NC^+$	$1.06 \times 10^{-9} [0.62 + 2.77(300K/T)^{0.5}]$	$\text{cm}^3 \text{s}^{-1}$	<i>b</i>
$H_2CNC + H^+ \rightarrow H + CH_2NC^+$	$4.94 \times 10^{-9} [0.62 + 2.77(300K/T)^{0.5}]$	$\text{cm}^3 \text{s}^{-1}$	<i>b</i>
$CH_3CN + He^+ \rightarrow He + CN^+ + CH_3$	$1.27 \times 10^{-9} [0.62 + 3.14(300K/T)^{0.5}]$	$\text{cm}^3 \text{s}^{-1}$	<i>a,c</i>
$CH_3CN + He^+ \rightarrow He + CH_3^+ + CN$	$1.27 \times 10^{-9} [0.62 + 3.14(300K/T)^{0.5}]$	$\text{cm}^3 \text{s}^{-1}$	<i>a,c</i>
$CH_3CN + H_3^+ \rightarrow H_2 + CH_3CNH^+$	$4.84 \times 10^{-9} [0.62 + 3.14(300K/T)^{0.5}]$	$\text{cm}^3 \text{s}^{-1}$	<i>a,c</i>
$CH_3CN + C^+ \rightarrow CN + C_2H_3^+$	$7.94 \times 10^{-10} [0.62 + 3.14(300K/T)^{0.5}]$	$\text{cm}^3 \text{s}^{-1}$	<i>a,c</i>
$CH_3CN + C^+ \rightarrow H + HC_2NCH^+$	$7.94 \times 10^{-10} [0.62 + 3.14(300K/T)^{0.5}]$	$\text{cm}^3 \text{s}^{-1}$	<i>a,c</i>
$CH_3CN + HCO^+ \rightarrow CO + CH_3CNH^+$	$1.17 \times 10^{-9} [0.62 + 3.14(300K/T)^{0.5}]$	$\text{cm}^3 \text{s}^{-1}$	<i>a,c</i>
$CH_3CN + H_3O^+ \rightarrow H_2O + CH_3CNH^+$	$1.34 \times 10^{-9} [0.62 + 3.14(300K/T)^{0.5}]$	$\text{cm}^3 \text{s}^{-1}$	<i>a,c</i>
$CH_3CN + HOCO^+ \rightarrow CO_2 + CH_3CNH^+$	$1.05 \times 10^{-9} [0.62 + 3.14(300K/T)^{0.5}]$	$\text{cm}^3 \text{s}^{-1}$	<i>a,c</i>
$CH_3CN + H^+ \rightarrow H_2 + CH_2CN^+$	$2.44 \times 10^{-9} [0.62 + 3.14(300K/T)^{0.5}]$	$\text{cm}^3 \text{s}^{-1}$	<i>a,c</i>
$CH_3CN + H^+ \rightarrow H + CH_3CN^+$	$2.44 \times 10^{-9} [0.62 + 3.14(300K/T)^{0.5}]$	$\text{cm}^3 \text{s}^{-1}$	<i>a,c</i>
$CH_3NC + He^+ \rightarrow He + CH_3^+ + CN$	$1.27 \times 10^{-9} [0.62 + 3.00(300K/T)^{0.5}]$	$\text{cm}^3 \text{s}^{-1}$	<i>a,c</i>
$CH_3NC + He^+ \rightarrow He + CH_3 + CN^+$	$1.27 \times 10^{-9} [0.62 + 3.00(300K/T)^{0.5}]$	$\text{cm}^3 \text{s}^{-1}$	<i>a,c</i>
$CH_3NC + H_3^+ \rightarrow H_2 + CH_3NCH^+$	$4.84 \times 10^{-9} [0.62 + 3.00(300K/T)^{0.5}]$	$\text{cm}^3 \text{s}^{-1}$	<i>a,c</i>
$CH_3NC + C^+ \rightarrow CN + C_2H_3^+$	$7.93 \times 10^{-10} [0.62 + 3.00(300K/T)^{0.5}]$	$\text{cm}^3 \text{s}^{-1}$	<i>a,c</i>
$CH_3NC + C^+ \rightarrow H + HC_2NCH^+$	$7.93 \times 10^{-10} [0.62 + 3.00(300K/T)^{0.5}]$	$\text{cm}^3 \text{s}^{-1}$	<i>a,c</i>

$\text{CH}_3\text{NC} + \text{HCO}^+ \rightarrow \text{CO} + \text{CH}_3\text{NCH}^+$	$1.17 \times 10^{-9} [0.62 + 3.00(300\text{K}/\text{T})^{0.5}]$	$\text{cm}^3 \text{s}^{-1}$	a,c
$\text{CH}_3\text{NC} + \text{H}_3\text{O}^+ \rightarrow \text{H}_2\text{O} + \text{CH}_3\text{NCH}^+$	$1.34 \times 10^{-9} [0.62 + 3.00(300\text{K}/\text{T})^{0.5}]$	$\text{cm}^3 \text{s}^{-1}$	a,c
$\text{CH}_3\text{NC} + \text{HOCO}^+ \rightarrow \text{CO}_2 + \text{CH}_3\text{NCH}^+$	$1.04 \times 10^{-9} [0.62 + 3.00(300\text{K}/\text{T})^{0.5}]$	$\text{cm}^3 \text{s}^{-1}$	a,c
$\text{CH}_3\text{NC} + \text{H}^+ \rightarrow \text{H}_2 + \text{CH}_2\text{NC}^+$	$2.44 \times 10^{-9} [0.62 + 3.00(300\text{K}/\text{T})^{0.5}]$	$\text{cm}^3 \text{s}^{-1}$	a,c
$\text{CH}_3\text{NC} + \text{H}^+ \rightarrow \text{H} + \text{CH}_3\text{NC}^+$	$2.44 \times 10^{-9} [0.62 + 3.00(300\text{K}/\text{T})^{0.5}]$	$\text{cm}^3 \text{s}^{-1}$	a,c
$\text{CH}_3\text{NC} + \text{H} \rightarrow \text{CH}_3 + \text{HCN}$	$e^{-1200\text{K}/\text{T}}$	$\text{cm}^3 \text{s}^{-1}$	b
$\text{CO} + \text{CH}_3\text{NC}^+ \rightarrow \text{H}_2\text{CNC} + \text{HCO}^+$	$8.03 \times 10^{-10} [1 + 0.024(300\text{K}/\text{T})^{0.5} + 0.006(300\text{K}/\text{T})^{-1}]$	$\text{cm}^3 \text{s}^{-1}$	b
$\text{CO} + \text{CH}_3\text{NC}^+ \rightarrow \text{H}_2\text{CCN} + \text{HCO}^+$	$8.03 \times 10^{-10} [1 + 0.024(300\text{K}/\text{T})^{0.5} + 0.006(300\text{K}/\text{T})^{-1}]$	$\text{cm}^3 \text{s}^{-1}$	b
$\text{CO} + \text{CH}_3\text{CN}^+ \rightarrow \text{H}_2\text{CNC} + \text{HCO}^+$	$8.03 \times 10^{-10} [1 + 0.024(300\text{K}/\text{T})^{0.5} + 0.006(300\text{K}/\text{T})^{-1}]$	$\text{cm}^3 \text{s}^{-1}$	b
$\text{CN} + \text{CH}_3 \rightarrow \text{CH}_3\text{NC} + \text{Photon}$	2.86×10^{-17}	$\text{cm}^3 \text{s}^{-1}$	a,b
$\text{HNC} + \text{CH}_3^+ \rightarrow \text{CH}_3\text{NCH}^+ + \text{Photon}$	$9.00 \times 10^{-9} (\text{T}/300\text{K})^{-0.5}$	$\text{cm}^3 \text{s}^{-1}$	d
$\text{CH}_3 + \text{CN}^- \rightarrow \text{CH}_3\text{NC} + \text{e}^-$	1.00×10^{-9}	$\text{cm}^3 \text{s}^{-1}$	b
$\text{CH}_2\text{OH} + \text{C}_2\text{H}_4\text{CN} \rightarrow \text{C}_2\text{H}_5\text{CN} + \text{H}_2\text{CO}$	1.00×10^{-11}	$\text{cm}^3 \text{s}^{-1}$	e
$\text{CH}_2\text{OH} + \text{C}_2\text{H}_4\text{NC} \rightarrow \text{C}_2\text{H}_5\text{NC} + \text{H}_2\text{CO}$	1.00×10^{-11}	$\text{cm}^3 \text{s}^{-1}$	e
$\text{CH}_2\text{OH} + \text{CH}_3\text{CHCN} \rightarrow \text{C}_2\text{H}_5\text{CN} + \text{H}_2\text{CO}$	1.00×10^{-11}	$\text{cm}^3 \text{s}^{-1}$	e
$\text{CH}_2\text{OH} + \text{CH}_3\text{CHNC} \rightarrow \text{C}_2\text{H}_5\text{NC} + \text{H}_2\text{CO}$	1.00×10^{-11}	$\text{cm}^3 \text{s}^{-1}$	e
$\text{CH}_3\text{O} + \text{C}_2\text{H}_4\text{CN} \rightarrow \text{C}_2\text{H}_5\text{CN} + \text{H}_2\text{CO}$	1.00×10^{-11}	$\text{cm}^3 \text{s}^{-1}$	e
$\text{CH}_3\text{O} + \text{C}_2\text{H}_4\text{NC} \rightarrow \text{C}_2\text{H}_5\text{NC} + \text{H}_2\text{CO}$	1.00×10^{-11}	$\text{cm}^3 \text{s}^{-1}$	e
$\text{CH}_3\text{O} + \text{CH}_3\text{CHCN} \rightarrow \text{C}_2\text{H}_5\text{CN} + \text{H}_2\text{CO}$	1.00×10^{-11}	$\text{cm}^3 \text{s}^{-1}$	e
$\text{CH}_3\text{O} + \text{CH}_3\text{CHNC} \rightarrow \text{C}_2\text{H}_5\text{NC} + \text{H}_2\text{CO}$	1.00×10^{-11}	$\text{cm}^3 \text{s}^{-1}$	e
$\text{HCO} + \text{C}_2\text{H}_4\text{CN} \rightarrow \text{C}_2\text{H}_5\text{CN} + \text{CO}$	1.00×10^{-11}	$\text{cm}^3 \text{s}^{-1}$	e
$\text{HCO} + \text{C}_2\text{H}_4\text{NC} \rightarrow \text{C}_2\text{H}_5\text{NC} + \text{CO}$	1.00×10^{-11}	$\text{cm}^3 \text{s}^{-1}$	e
$\text{HCO} + \text{CH}_3\text{CHCN} \rightarrow \text{C}_2\text{H}_5\text{CN} + \text{CO}$	1.00×10^{-11}	$\text{cm}^3 \text{s}^{-1}$	e
$\text{HCO} + \text{CH}_3\text{CHNC} \rightarrow \text{C}_2\text{H}_5\text{NC} + \text{CO}$	1.00×10^{-11}	$\text{cm}^3 \text{s}^{-1}$	e
Grain-Surface Reaction	Activation Energy [K]		Reference
$\text{CH}_2\text{OH} + \text{C}_2\text{H}_4\text{CN} \rightarrow \text{C}_2\text{H}_5\text{CN} + \text{H}_2\text{CO}$	0		e
$\text{CH}_2\text{OH} + \text{C}_2\text{H}_4\text{NC} \rightarrow \text{C}_2\text{H}_5\text{NC} + \text{H}_2\text{CO}$	0		e
$\text{CH}_2\text{OH} + \text{C}_2\text{H}_5\text{CN} \rightarrow \text{CH}_3\text{OH} + \text{C}_2\text{H}_4\text{CN}$	6490		e
$\text{CH}_2\text{OH} + \text{C}_2\text{H}_5\text{NC} \rightarrow \text{CH}_3\text{OH} + \text{C}_2\text{H}_4\text{NC}$	6490		e
$\text{CH}_2\text{OH} + \text{C}_2\text{H}_5\text{CN} \rightarrow \text{CH}_3\text{OH} + \text{CH}_3\text{CHCN}$	5990		e
$\text{CH}_2\text{OH} + \text{C}_2\text{H}_5\text{NC} \rightarrow \text{CH}_3\text{OH} + \text{CH}_3\text{CHNC}$	5990		e
$\text{CH}_2\text{OH} + \text{H}_2\text{CCN} \rightarrow \text{CH}_3\text{CN} + \text{H}_2\text{CO}$	0		e
$\text{CH}_2\text{OH} + \text{H}_2\text{CNC} \rightarrow \text{CH}_3\text{NC} + \text{H}_2\text{CO}$	0		e
$\text{CH}_2\text{OH} + \text{CH}_3\text{CN} \rightarrow \text{CH}_3\text{OH} + \text{H}_2\text{CCN}$	6200		e
$\text{CH}_2\text{OH} + \text{CH}_3\text{NC} \rightarrow \text{CH}_3\text{OH} + \text{H}_2\text{CNC}$	6200		e
$\text{CH}_2\text{OH} + \text{CH}_3\text{CHCN} \rightarrow \text{H}_2\text{CO} + \text{C}_2\text{H}_5\text{CN}$	0		e
$\text{CH}_2\text{OH} + \text{CH}_3\text{CHNC} \rightarrow \text{H}_2\text{CO} + \text{C}_2\text{H}_5\text{NC}$	0		e
$\text{CH}_3 + \text{H}_2\text{CCN} \rightarrow \text{C}_2\text{H}_5\text{CN}$	0		e
$\text{CH}_3 + \text{H}_2\text{CNC} \rightarrow \text{C}_2\text{H}_5\text{NC}$	0		e
$\text{CH}_3\text{O} + \text{C}_2\text{H}_4\text{CN} \rightarrow \text{C}_2\text{H}_5\text{CN} + \text{H}_2\text{CO}$	0		e
$\text{CH}_3\text{O} + \text{C}_2\text{H}_4\text{NC} \rightarrow \text{C}_2\text{H}_5\text{NC} + \text{H}_2\text{CO}$	0		e
$\text{CH}_3\text{O} + \text{C}_2\text{H}_5\text{CN} \rightarrow \text{C}_2\text{H}_4\text{CN} + \text{CH}_3\text{OH}$	2340		e
$\text{CH}_3\text{O} + \text{C}_2\text{H}_5\text{NC} \rightarrow \text{C}_2\text{H}_4\text{NC} + \text{CH}_3\text{OH}$	2340		e
$\text{CH}_3\text{O} + \text{C}_2\text{H}_5\text{CN} \rightarrow \text{CH}_3\text{CHCN} + \text{CH}_3\text{OH}$	1950		e
$\text{CH}_3\text{O} + \text{C}_2\text{H}_5\text{NC} \rightarrow \text{CH}_3\text{CHNC} + \text{CH}_3\text{OH}$	1950		e
$\text{CH}_3\text{O} + \text{H}_2\text{CCN} \rightarrow \text{CH}_3\text{CN} + \text{H}_2\text{CO}$	0		e
$\text{CH}_3\text{O} + \text{H}_2\text{CNC} \rightarrow \text{CH}_3\text{NC} + \text{H}_2\text{CO}$	0		e
$\text{CH}_3\text{O} + \text{CH}_3\text{CN} \rightarrow \text{CH}_3\text{OH} + \text{H}_2\text{CCN}$	2070		e
$\text{CH}_3\text{O} + \text{CH}_3\text{NC} \rightarrow \text{CH}_3\text{OH} + \text{H}_2\text{CNC}$	2070		e
$\text{CH}_3\text{O} + \text{CH}_3\text{CHCN} \rightarrow \text{C}_2\text{H}_5\text{CN} + \text{H}_2\text{CO}$	0		e
$\text{CH}_3\text{O} + \text{CH}_3\text{CHNC} \rightarrow \text{C}_2\text{H}_5\text{NC} + \text{H}_2\text{CO}$	0		e
$\text{H} + \text{C}_2\text{H}_2\text{CN} \rightarrow \text{CH}_2\text{CHCN}$	0		e
$\text{H} + \text{C}_2\text{H}_2\text{NC} \rightarrow \text{C}_2\text{H}_3\text{NC}$	0		e
$\text{H} + \text{CH}_2\text{CHCN} \rightarrow \text{C}_2\text{H}_4\text{CN}$	1320		e
$\text{H} + \text{C}_2\text{H}_3\text{NC} \rightarrow \text{C}_2\text{H}_4\text{NC}$	1320		e
$\text{H} + \text{CH}_2\text{CHNC} \rightarrow \text{CH}_3\text{CHCN}$	619		e
$\text{H} + \text{C}_2\text{H}_3\text{NC} \rightarrow \text{CH}_3\text{CHNC}$	619		e
$\text{H} + \text{C}_2\text{H}_4\text{CN} \rightarrow \text{C}_2\text{H}_5\text{CN}$	0		e
$\text{H} + \text{C}_2\text{H}_4\text{NC} \rightarrow \text{C}_2\text{H}_5\text{NC}$	0		e
$\text{H} + \text{CH}_3\text{CHCN} \rightarrow \text{C}_2\text{H}_5\text{CN}$	0		e
$\text{H} + \text{CH}_3\text{CHNC} \rightarrow \text{C}_2\text{H}_5\text{NC}$	0		e

$H + H_2CNC \rightarrow CH_3NC$	0	<i>b</i>
$H + CH_3CN \rightarrow HCN + CH_3$	1200	<i>e</i>
$H + CH_3NC \rightarrow HCN + CH_3$	1200	<i>e</i>
$H + HC_3N \rightarrow C_2H_2CN$	1710	<i>e</i>
$H + HCCNC \rightarrow C_2H_2NC$	1710	<i>e</i>
$H + HCN \rightarrow H + HNC$	0	<i>e</i>
$H + HNC \rightarrow H + HCN$	1200	<i>e</i>
$H_2CCN + CH_2 \rightarrow C_2H_4CN$	0	<i>e</i>
$H_2CNC + CH_2 \rightarrow C_2H_4NC$	0	<i>e</i>
$HCO + C_2H_4CN \rightarrow C_2H_5CN + CO$	0	<i>e</i>
$HCO + C_2H_4NC \rightarrow C_2H_5NC + CO$	0	<i>e</i>
$HCO + H_2CCN \rightarrow CH_3CN + CO$	0	<i>e</i>
$HCO + H_2CNC \rightarrow CH_3NC + CO$	0	<i>e</i>
$HCO + CH_3CHCN \rightarrow C_2H_5CN + CO$	0	<i>e</i>
$HCO + CH_3CHNC \rightarrow C_2H_5NC + CO$	0	<i>e</i>
$HOCO + C_2H_4CN \rightarrow C_2H_5CN + CO_2$	0	<i>e</i>
$HOCO + C_2H_4NC \rightarrow C_2H_5NC + CO_2$	0	<i>e</i>
$HOCO + H_2CCN \rightarrow CH_3CN + CO_2$	0	<i>e</i>
$HOCO + H_2CNC \rightarrow CH_3NC + CO_2$	0	<i>e</i>
$HOCO + CH_3CHCN \rightarrow C_2H_5CN + CO_2$	0	<i>e</i>
$HOCO + CH_3CHNC \rightarrow C_2H_5NC + CO_2$	0	<i>e</i>
$NH + C_2H_5CN \rightarrow NH_2 + C_2H_4CN$	7200	<i>e</i>
$NH + C_2H_5NC \rightarrow NH_2 + C_2H_4NC$	7200	<i>e</i>
$NH + C_2H_5CN \rightarrow NH_2 + CH_3CHCN$	7000	<i>e</i>
$NH + C_2H_5NC \rightarrow NH_2 + CH_3CHNC$	7000	<i>e</i>
$NH + CH_3CN \rightarrow NH_2 + H_2CCN$	7000	<i>e</i>
$NH + CH_3NC \rightarrow NH_2 + H_2CNC$	7000	<i>e</i>
$NH_2 + C_2H_5CN \rightarrow NH_3 + C_2H_4CN$	3280	<i>e</i>
$NH_2 + C_2H_5NC \rightarrow NH_3 + C_2H_4NC$	3280	<i>e</i>
$NH_2 + C_2H_5CN \rightarrow NH_3 + CH_3CHCN$	2480	<i>e</i>
$NH_2 + C_2H_5NC \rightarrow NH_3 + CH_3CHNC$	2480	<i>e</i>
$NH_2 + CH_3CN \rightarrow NH_3 + H_2CCN$	2680	<i>e</i>
$NH_2 + CH_3NC \rightarrow NH_3 + H_2CNC$	2680	<i>e</i>
$O + HNC \rightarrow CO + NH$	1100	<i>e</i>
$O + HCN \rightarrow CO + NH$	1100	<i>b</i>
$OH + C_2H_5CN \rightarrow H_2O + C_2H_4CN$	1200	<i>e</i>
$OH + C_2H_5NC \rightarrow H_2O + C_2H_4NC$	1200	<i>e</i>
$OH + C_2H_5CN \rightarrow H_2O + CH_3CHCN$	1000	<i>e</i>
$OH + C_2H_5NC \rightarrow H_2O + CH_3CHNC$	1000	<i>e</i>
$OH + CH_2CHCN \rightarrow H_2O + C_2H_2CN$	4000	<i>e</i>
$OH + C_2H_3NC \rightarrow H_2O + C_2H_2NC$	4000	<i>e</i>
$OH + CH_3CN \rightarrow H_2O + H_2CCN$	500	<i>e</i>
$OH + CH_3NC \rightarrow H_2O + H_2CNC$	500	<i>e</i>

^(a) this work

^(b) from analogous cyanide reaction

^(c) method from [Woon & Herbst \(2009\)](#)

^(d) [Anicich et al. \(1994\)](#)

^(e) [Willis et al. \(2020\)](#)

^(f) predicted products of photodestruction

*In reaction rate formulae: ζ is the H_2 cosmic-ray ionization rate; A_v is the visual extinction.

This paper has been typeset from a \LaTeX file prepared by the author.